Advances in Water Resources 174 (2023) 104420

Contents lists available at ScienceDirect

Advances in Water Resources

journal homepage: www.elsevier.com/locate/advwatres

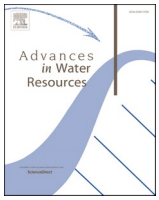

Multiscale pore-fracture hybrid pore network modeling for drainage in tight carbonate

Zhipeng Xu [a], Mian Lin [b,c,*], Lili Ji [b,c], Wenbin Jiang [b,c], Gaohui Cao [b], Leige Xu [a]

[a] School of Civil Engineering and Communication, North China University of Water Resources and Electric Power, Zhengzhou 450045, China
[b] Chinese Academy of Sciences, Institute of Mechanics, Beijing 100190, China
[c] School of Engineering Science, University of Chinese Academy of Sciences, Beijing 100049, China

ARTICLE INFO

Keywords:
Multiscale pores
Fractures
Multiscale hybrid pore network modeling
Two-phase flow
Tight carbonate

ABSTRACT

Tight carbonate possesses both fractures and multiscale pores. Flow through tight carbonate rocks involves several length scales and the complicated flow physics. Capturing and modeling the entire void space into a single pore network model for drainage is challenging. Here, we present a novel method for modeling of a multiscale pore-fracture hybrid pore network, which enables various void spaces at multiple length scales and the flow characteristics in them to be included. Pores and fractures in a low-resolution CT image are extracted by medial axis-maximal ball algorithm and medial surface algorithm, respectively, to generate a pore-fracture hybrid pore network. Then, a statistics-based small-scale stochastic pore network is established in the CT image solid domains to represent the micropores unresolved by the image. The two pore networks are organically integrated into a multiscale hybrid pore network by cross-scale connections. The statistics of small-scale pore network are determined by experimental permeability. We study the effects of the small-scale pore network density on connectivity, single- and two-phase flow properties of the model to obtain the robust parameter. The influence of fractures on two-phase flow properties is analyzed. Results show the significance of incorporating fractures and micropores in the model. The model is validated via comparison between simulation result and experimental data. This method can accurately, efficiently, conveniently construct multiscale pore-fracture hybrid pore network of tight carbonate rock for evaluating the drainage characteristics.

1. Introduction

Tight carbonate rocks exhibit complex void structure with heterogeneities due to the presence of fractures and multiscale pores. The multi-stages and multi-types flow channels have a significant influence on fluid flow, such as the slip effect in nanometer pores and the interaction between the fractures and adjacent pores. Transport processes of fluid in tight carbonate rocks actually occur at the pore-scale, and the pore scale simulation helps to understand the flow behavior and obtain flow properties at large scales (Jiang et al., 2013; Pak et al., 2014; Rabbani et al., 2020). The key is acquiring and modeling the entire representative void structures into a computationally tractable model.

With the rapid progress in imaging techniques, such as micro-computed-tomography (μCT) imaging and focused ion beam scanning electron microscopy (FIB-SEM) imaging (Arns et al., 2005; Tomutsa et al., 2007; Müter et al., 2012, 2014; Gooya et al., 2016), the 3D representation of the void space can be implemented. Pore network model (PNM) extracted from the 3D image has been extensively applied to simulate single- and two-phase flow because it is computationally more efficient than direct models (e.g., CFD-DEM model) without sacrificing too much accuracy (Blunt et al., 2013; Li et al., 2021). Less computational demands also allow PNM to be competent for larger rock image to consider more heterogeneity of void structure. However, for heterogeneous tight carbonate rocks, two vital problems remain for PNM. First, the multiscale pore size ranges from several nanometers to hundreds of microns (Tan et al., 2020), resulting in the inability of a single image to cover all void spaces. PNM extracted from a low-resolution image has no global permeability due to the lacks of micropores unresolved by the image, while PNM extracted from a small high-resolution image might not be representative. Secondly, fracture exhibits the complicated morphology and topology. Modeling and coupling the fracture into a PNM for calculating fluid exchange between the fracture network and adjacent pores are challenging. The presence of multiscale pores and fractures, the resolution/size trade-off, and the pore space-fracture interaction make it necessary to model a multiscale pore-fracture

* Corresponding author at: Chinese Academy of Sciences, Institute of Mechanics, Beijing 100190, China.
E-mail address: linmian@imech.ac.cn (M. Lin).

https://doi.org/10.1016/j.advwatres.2023.104420
Received 9 December 2022; Received in revised form 24 February 2023; Accepted 14 March 2023
Available online 16 March 2023

Nomenclature

N_{SP}	the number of pores in NET_{small}
f_S	adjustable coefficient of NET_{small}
V_S	volume of NET_{small}
ρ_{SP}	density of the extracted small-scale pore network
I_{core}	low-resolution 3D image of tight carbonate
SS	search sphere
SSe	a set contains the voxels from the center to the farthest within the search radius
NET_{large}	large-scale pore network extracted from I_{core}
NET_{small}	small-scale stochastic pore network
ρ_{LP}	pore density of NET_{large}
N_{LP}	the number of pores in NET_{large}
V_L	volume of NET_{large}
NET_{multi}	multiscale pore-fracture hybrid pore network
$d_t(p_1,p_2)$	distance between pore p_1 and pore p_2
$d_e(p_1,p_2)$	Euclidean distance between pore p_1 and pore p_2
r_1	radius of pore p_1
r_2	radius of pore p_2
$\widetilde{d}_t$	maximum length of throats in NET_{small}
$p_{LPP,i}$	the i th large-scale pore in NET_{large}
N_{LPP}	the number of large-scale pores in NET_{large}
$p_{SP,ii}$	the ii-th pore in NET_{small}
$N_{SP,i}$	the number of pores in NET_{small} satisfying $d_t(p_{LPP,i}, p_{SP,ii}) \le \widetilde{d}_t$
γ_S	parameter representing the density and connectivity of NET_{small}
c_S	center of NET_{small}
ξ	the number of concentric spheres in NET_{small}
$N_{ST,k}$	the number of throats penetrating the k-th concentric sphere in NET_{small}
R_k	radius of k-th concentric sphere
$t_{ST,j}$	the j-th throat in NET_{small}
N_{ST}	the number of throats in NET_{small}
$p_{SP,j1}$	pore connected to one end of throat $t_{ST,j}$
$p_{SP,j2}$	pore connected to the other end of throat $t_{ST,j}$
a_k	surface area of the k-th concentric sphere
$r_{LPP,i}$	radius of $p_{LPP,i}$
$CN_{LPP,i}$	coordination number of $p_{LPP,i}$
$t_{LPT,ij}$	large-scale throat connecting $p_{LPP,i}$ and $p_{LPP,j}$ in NET_{large}
$r_{LPT,ij}$	radius of $t_{LPT,ij}$
$a_{LPT,ij}$	area of spherical crown occupied by $t_{LPT,ij}$
$sa_{LPP,i}$	remaining surface are of $p_{LPP,i}$
$SCN_{LPP,i}$	the number of pores of NET_{small} that can be connected to $p_{LPP,i}$
p_{LFP}	fracture pore in NET_{large}
$q_{f,ij}$	flow flux of phase f in throat ij
$P_{f,i}$	pressure of phase f in pore i
$P_{f,j}$	pressure of phase f in pore j
$g_{f,ij}$	hydraulic conductivity of phase f in throat ij
A_{ij}	cross sectional area of throat ij
l_{ij}	length of throat ij
G_{ij}	shape factor of cross section of throat ij
μ_f	viscosity of phase f
Ld_{ij}	dimensionless slip length of liquid flow in throat ij
Ls_{ij}	physical slip length of liquid flow in throat ij
$t_{LFT,ij}$	fracture throat connecting $p_{LFP,i}$ and $p_{LFP,j}$
$w_{F,ij}$	width of $t_{LFT,ij}$
$h_{F,ij}$	equivalent aperture of $t_{LFT,ij}$
$l_{F,ij}$	length of $t_{LFT,ij}$
$P_{in,t}$	inlet pressure of NET_{multi} at the t-th iteration step
P_{out}	outlet pressure of NET_{multi}
$Q_{f,in}$	total flow flux of phase f at the inlet interface of NET_{multi}
$Q_{f,k}$	flow flux of phase f in the k-th inlet pore
$Q_{f,out}$	total flow flux of phase f at the outlet interface of NET_{multi}
Q_f	total flow flux of phase f
L	vertical distance between the inlet interface and the outlet interface of NET_{multi}
A	area of the inlet interface of NET_{multi}
K_{mf}	absolute permeability of phase f
K_{sf}	absolute permeability of phase f under the single-phase flow
K_{rf}	relative permeability
P_c	capillary pressure

hybrid pore network for drainage in the entire void space of tight carbonate rocks.

PNM is the foundation of this study. PNM can be extracted from the binarized image of a pore space, in which the irregular pore space is represented by a simple network of interconnected pores and throats. There are some PNM extraction methods including medial axis (MA) method (Lindquist and Lee, 1996; Jiang et al., 2007), maximal ball (MB) method (Silin et al., 2003; Dong and Blunt, 2009), watershed segmentation (WS) method (Rabbani et al., 2014, 2019), pore throat morphology (PTM) method (Xu et al., 2020), and medial axis-maximal ball (AB) method (Yi et al., 2017; Jiang et al., 2017a). AB method combines the advantages of MA and MB to constrain the maximal balls on the centrally located medial axis, which can preserve most of the morphological features of the pore space and has been successfully proven to be highly realistic and efficient in some studies (Yi et al., 2017; Jiang et al., 2017b; Cao et al., 2017).

Then, for the binarized image containing both fractures and pore spaces, there is a need to extract a pore-fracture hybrid pore network from it to include the pore-fracture interactions and achieve the globally single- and two-phase flow simulations. The process involves two important questions: how to identify and model the fractures to couple with the pore spaces, and how to achieve simulations of fluid exchange between fractures and adjacent pores. For the first question, Pruess and Tsang (1990) and Karpyn and Piri (2007) used a dense network consisting of virtual pores and throats to represent a fracture, and simulated single- and two-phase flow in the network. Regions with local maxima of the fracture aperture are defined as virtual pores, which are connected by virtual throats defined by other fracture regions. Later, Hughes and Blunt (2001) and Erzeybek and Akin (2008) plugged virtual networks of fractures into a regular pore network and used throats to connect the virtual networks with nearby pores. Recently, Jiang et al. (2017a) presented a generally applicable method to extract a pore-fracture hybrid pore network from the actual fractured porous media image. Since the actual fracture possesses the complicated platy morphology, the medial surface (MS) is the best representation of the fracture (Lee et al., 1994), which is defined as a set of surface voxels that are essential for the topology and connectivity of fracture. They used MA method to extract skeleton of pore system, and used an extended shrinking algorithm to identify the fracture and extract the corresponding MS. MS was subsequently converted into a dense network consisting of virtual medial axes. The entire skeleton was transformed into a hybrid pore network by defining vertices and links as pores and throats. For the second important question of how to simulate fluid exchange between fractures and adjacent pores, the hybrid pore network has significant computational advantages. All void components (pore system and fractures) in the hybrid pore network are represented by the same basic elements: pores

and throats, which can be calculated by the same simulator.

Further, for some porous media with the multiscale pore spaces, the multiscale pore network model has been proposed. The fundamental idea of that is extracting a large-scale pore network from a low-resolution 3D image and integrating it with the micropore networks generated from other sources into a single multiscale pore network. Jiang et al. (2013) presented a method for fusing pore networks extracted from μCT images of different resolutions into a multiscale pore network via the cross-scale connection structures. Since the domain of the extracted small-scale pore network is smaller than that of the extracted large-scale pore network, the micropore network was randomly reestablished in a domain of the same size as the large-scale pore network, based on the statistical information of the extracted small-scale pore network. To control the density of micropore networks for efficient flow simulation, a parameter $0 < f_S < 1$ was introduced to determine the number of micropores:

$$N_{SP} = f_S \rho_{SP} V_S \tag{1}$$

where N_{SP} is the number of micropores, ρ_{SP} is the density of the extracted small-scale pore network, V_S is the volume of micropore network. Later, the method was revised by considering the locations of micropore networks (Mehmani and Prodanović, 2014; Prodanović et al., 2014; Tahmasebi and Kamrava, 2018). They proposed that micropores in rocks are generated due to the partial dissolution of some solid matrix particles and the filling of some macropores by clay particles. The micropore networks were placed in some matrix regions (grain filling) and some macropores (pore filling). Mehmani and Prodanović (2014) and Prodanović et al. (2014) generated micropore networks by rescaling the extracted large-scale pore network, implying that some characteristics (e.g., tortuosity, coordination number distribution, shape factor distribution) of large-scale pores were used to represent the micropores. Tahmasebi and Kamrava (2018) extracted micropore networks from 3D digital cores reconstructed based on different regions of a SEM image. Additionally, some researchers (Bauer et al., 2012; Bultreys et al., 2015; Xu et al., 2021) used the micro-links to represent the micropores and connect macropore network clusters to generate the multiscale pore network.

However, tight carbonate has both fractures and multiscale pore spaces, which is quite complicated. To the best of our knowledge, there are few relevant studies on the multiscale hybrid pore network models for the entire void structures of tight carbonate rocks. Rabbani et al. (2020) constructed a triple pore network containing micropores, meso-pores, and fractures, and simulated the gas transport in it. Here, we present a novel method to construct a multiscale pore-fracture hybrid pore network model for drainage in tight carbonate rocks.

2. Methods

2.1. Multiscale pore-fracture hybrid pore network construction

2.1.1. Pore-fracture hybrid pore network extraction

We implement a combined algorithm of AB (Yi et al., 2017) and MS (Jiang et al., 2017a) to extract the hybrid pore network consisting of pores and fractures from the low-resolution 3D image (I_{core}) of tight carbonate. The fundamental principle of AB is constraining maximal balls on the centrally located medial axis, which combines the advantages of MA (Lindquist et al., 1996; Jiang et al., 2007) and MB (Silin et al., 2003; Dong and Blunt, 2009), and ensures that each throat is located at the hydraulic restriction. The MS is the extracted skeleton of fracture, which characterizes the topology and hydraulic property of fracture. The combined algorithm involves the following steps:

1 Building the inscribed sphere for each void voxel in the 3D image via a layer-by-layer search algorithm developed previously (Yi et al., 2017). A search sphere *SS* with a large search radius is established first, in which each element is a vector coordinate relative to the center of *SS* (see Fig. 1d and e, a simple *SS* and its norms in a 2D system). Assigning the *SS* to any void voxel *k*. $SSe = k + SS$ can be acquired, which contains the voxels from the voxel *k* to the farthest within the search radius. All voxels in *SSe* are checked one by one in the order of the distance to the voxel *k* from the small to large, until a solid voxel or boundary voxel is found. The inscribed sphere for each voxel is built and its radius is acquired.

2 A shrinking algorithm developed by Jiang et al. (2017a) is applied to identify both the MA of the pore spaces and the MS of the fractures. Starting from void voxels on the void space wall, through searching and removing the void voxels that do not affect the Euler number and local connectivity of the void space, we find the MA of the pore spaces (Fig. 1f) and the MS of the fractures (Fig. 1g). Especially, the inscribed spheres are also utilized to make the MA and the MS more centered. Fig. 1a and Fig. 1b highlight the scheme. MA of the pore spaces and MS of the fracture (Fig. 1b) are effectively extracted from the entire void space consisting of the pore spaces and the fracture (Fig. 1a).

3 For the pore spaces with MA:
   a) Identifying the inscribed spheres corresponding to the MA voxels and removing other inscribed spheres to constrain the maximal balls on the MA (Yi et al., 2017).
   b) Affiliating these maximal balls into family trees to defined pores and throats. According to the order of maximal ball radius from large to small, all maximal balls are clustered based on their radii and locations to determine the hierarchical relationships among them. From the hierarchical relationship, the family trees of all maximal balls are generated (Fig. 1h), in which the center of parent ball is defined as pore location and the center of common child ball attaching to two parent balls is defined as throat location (Yi et al., 2017).
   c) Segmenting pore blocks and throat blocks via a dual-speed expansion algorithm developed previously (Yi et al., 2017). All pore location voxels and throat location voxels are labeled with 0. Starting from the pore location voxels and the throat location voxels, pore blocks and throat blocks expand outward, and the unmarked void voxels involved are labeled with the number of expansions. Pore blocks expand two layers outward each time (Fig. 1i), and throat blocks expand one layer outward each time (Fig. 1j). The entire pore space is divided into a series of pore blocks and throat blocks.

4 For the fractures with MS, converting the MS into a dense network consisting of virtual medial axes (see Fig. 1k) to generate a dense network consisting of virtual pores and throats (Jiang et al., 2017a).

5 The parameters (e.g., shape factor, coordination number, etc.) of pores and throats that are associated with the pore spaces and the pore-fracture connecting spaces are calculated as usual (Yi et al., 2017). The parameters (e.g., width, equivalent aperture, etc.) of virtual pores and throats of the dense network are determined based on the underlying fracture apertures (Jiang et al., 2017a).

Finally, a hybrid pore network is generated to represent the entire void space, as shown in Fig. 1c. The entire extraction process is briefly introduced above, in which AB is applied to treat the pore spaces and MS is used to process the fractures. For more details about the hybrid pore network generation, one can refer to the aforementioned publication. Note that the extracted hybrid pore network in general has no global connectivity due to the lacks of micropores unresolved by I_{core}. For the remainder of this work, we refer to the hybrid pore network as large-scale network (NET_{large}), and refer to the pore and throat corresponding to pore spaces as large-scale pore and large-scale throat, and the pore and throat corresponding to fractures as fracture pore and fracture throat.

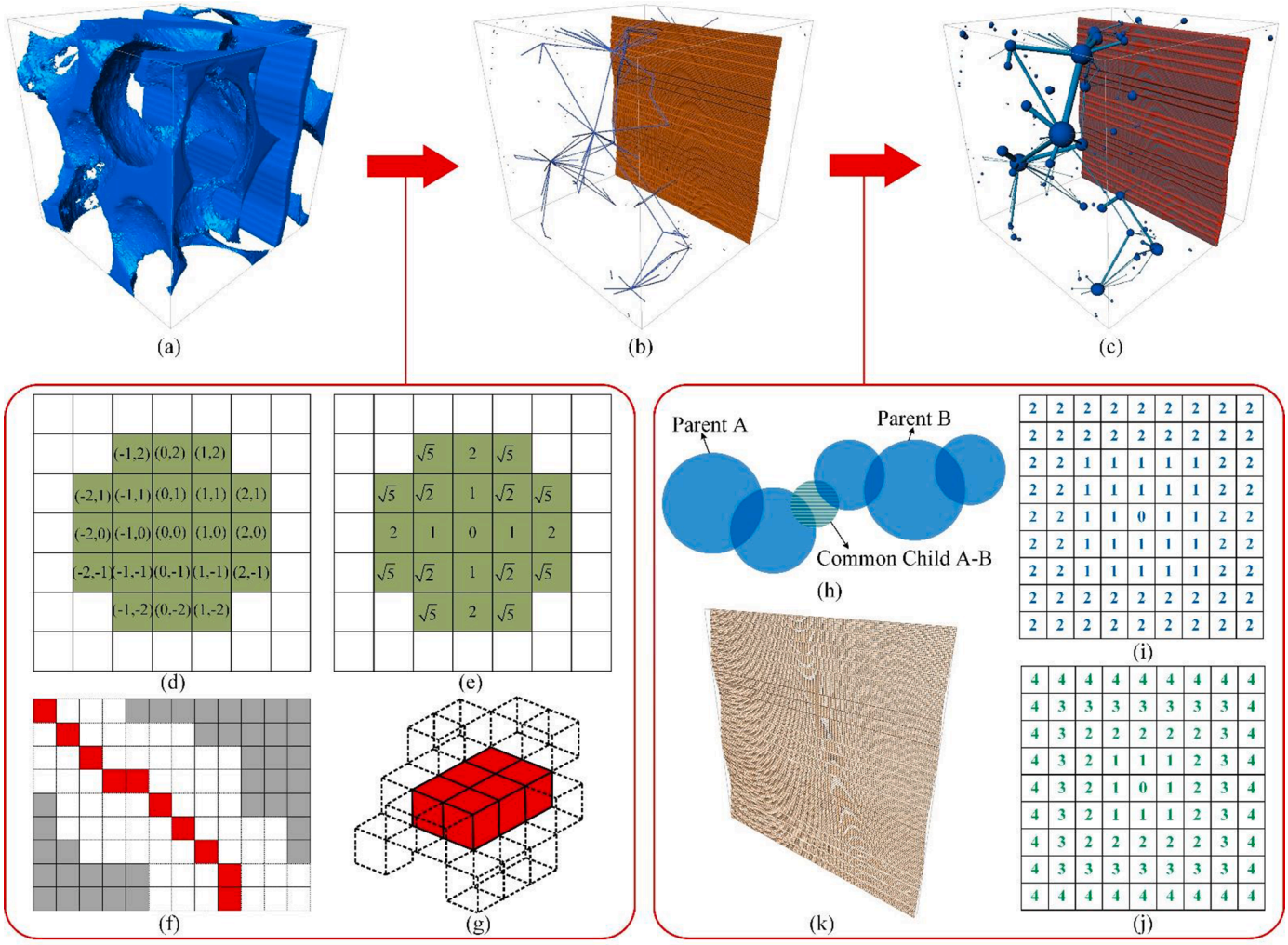

Fig. 1. (a) The entire void space of a porous media consists of the pore spaces and the fracture. (b) The hybrid skeleton extracted from the entire void space is composed of the medial axis (MA) of the pore spaces and the medial surface (MS) of the fracture. (c) The final pore-fracture hybrid pore network. (d) The search sphere (*SS*) consists of vector coordinates relative to the center of *SS* (Yi et al., 2017). (e) The norm set of *SS*. The search radius of *SS* is $\sqrt{5}$ in the schematic. (f) The schematic of extracting MA from pore spaces (Yi et al., 2017). Red represents the MA void voxels. Gray and white denote the solid voxels and the removed void voxels, respectively. (g) The schematic of extracting MS from fracture (Jiang et al., 2017). Red cube represents the MS void voxels, and the cube with dotted outlines denotes the removed void voxels. (h) The family trees of maximal balls for defining pore locations and throat locations. (i) The schematic of pore block expansion. (j) The schematic of throat block expansion. (k) The MS is converted to a dense network consisting of virtual medial axis.

2.1.2. Small-scale stochastic pore network generation

After the NET_{large} has been extracted from the I_{core}, we establish the small-scale stochastic pore network (NET_{small}) in the matrix domains of I_{core} to represent the micropores unresolved by I_{core} and supplement the NET_{large} with the connectivity generated by the micropores. The first step is determining the geometric and topological parameters of micropores. As mentioned above, Mehmani and Prodanović (2014) and Prodanović et al. (2014) generated the small-scale pore network by rescaling the macropore network, indicating that some characteristics of macropores were used to represent the small-scale pores. This is more economic and efficient compared with the scheme of extracting statistics of micropores from the high-resolution μCT image (Jiang et al., 2013) and the scheme of reconstructing 3D image of micropores based on SEM image (Tahmasebi and Kamrava, 2018), however, the uncertainty of the micropores is significant. Moreover, predictions of the multiscale model usually do not agree well with the experimental measurements due to the strong heterogeneity, and the multiscale model generally needs to be constrained and optimized by a kind of experiment data (Pak et al., 2016). Following the two ideas of Mehmani and Prodanović(2014) and Pak et al. (2016), we use some parameters (tortuosity, coordination number distribution, shape factor distribution) of large-scale pores and throats of the NET_{large} to represent the micropores. Then, we set the pore radius distribution and the throat radius distribution of micropores as the appropriate distributions and determine them under the constraint of experimental permeability to reduce the above uncertainty. The detail of the determination will be introduced in Section 2.1.3.3. Note that the maximum radius of the two distributions is given by the resolution of I_{core} and not by the minimum throat radius of the NET_{large}.

For the N_{SP} of the NET_{small}, we use Eq. (1) to determine it by replacing ρ_{SP} with ρ_{LP} based on the idea of Mehmani and Prodanović(2014). ρ_{LP} is pore density of NET_{large} and can be written as:

$$\rho_{LP} = \frac{N_{LP}}{V_L} \tag{2}$$

where N_{LP} is the number of pores in the NET_{large}, and V_L is the volume of the NET_{large}.

Next, we extend the algorithm proposed by Idowu and Blunt (2010) to generate a NET_{small} based on the given parameters. The major difference of our extended algorithm is that pores and throats are strictly confined in the irregular matrix domain. The producer is shown below.

1 Morphological dilation operation with radius of 2 voxel is implemented on the entire void space of the I_{core} (Xu et al., 2020) to transform the matrix within the range of 2 voxels around the void space into voids. The remaining matrix is the domain to establish the NET_{small}, as shown in Fig. 2 (a 2D slice of the pore-fractured porous media in Fig. 1a). Since the maximum radius of small-scale pores is the resolution of the I_{core}, even if the center of a small-scale pore is located at the edge of the residual matrix domain, it will not intersect with the pore spaces and fractures of the I_{core} (see Fig. 2)
2 N_{SP} pores are created by randomly assigning values of radius, shape factor, and coordination number to every pore based on the given distributions. The centers of these pores are randomly placed in the remaining matrix domain and make sure that there is no overlap of them. Then, the volume and weight are calculated for each pore (Idowu and Blunt, 2010; Xu et al., 2021).
3 Creating throats according to the coordination number of each pore to connect these pores (Idowu and Blunt, 2010). If the cylindrical throats intersect with the pore spaces and fractures of the I_{core}, we discard them and continue to find other connections for the corresponding pores (see Fig. 2). Therefore, the actual connection number of some pores may be less than their assigned coordination number due to the domain constraint.
4 Calculating the weight for every throat based on the weights of two pores connected to it (Idowu and Blunt, 2010; Xu et al., 2021). According to the given distributions, the smallest geometrical values (radius, shape factor) are assigned to the throat with the smallest weight, and the second smallest values are assigned to the throat with the second smallest weight, and so on, to ensure the correlation of the NET_{small}. Then, the length of each throat is calculated based on the center position and radius of two pores connected to it, and the volume is calculated for each throat (Idowu and Blunt, 2010).

In the end, the NET_{small} is generated. As described, the number of large-scale pores and throats in the NET_{large} should be enough to obtain the representative parameters (tortuosity, coordination number distribution, shape factor distribution) to generate the NET_{small}. However, if there are only a few pore spaces captured in the I_{core}, these parameters can also be obtained from other sources, for example, obtaining these parameters from the higher-resolution image via the pore-throats morphology (PTM) software we developed previously (Xu et al., 2020). The novel way provided to obtain the small-scale pore parameters is intended to be illustrative rather than the unique solution, because the central contribution of the paper is the multiscale pore-fracture hybrid pore network modeling and integration method.

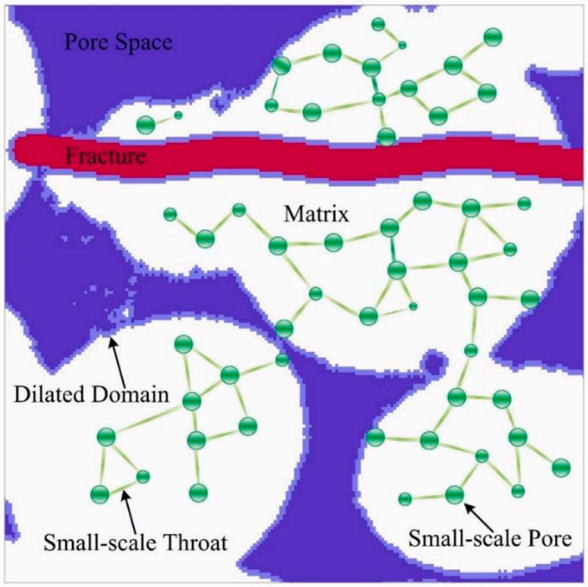

Fig. 2. A 2D slice of the pore-fractured porous media shown in Fig. 1a. The entire void space is dilated by a structuring element with radius of 2 voxel (Xu et al., 2020) to convert the matrix within the range of 2 voxels around the void space into voids. The remaining matrix (white) is the domain for the small-scale stochastic pore network.

2.1.3. Multiscale pore-fracture hybrid pore network generation

After obtaining the NET_{large} and the NET_{small}, the two pore networks are integrated into a multiscale pore-fracture hybrid pore network (NET_{multi}). The major idea of the process is connecting pores of NET_{large} and their nearby pores of NET_{small} via the added small-scale throats. In order to ensure that the final NET_{multi} is a correlated network in terms of geometry and topology, both the geometric and topological properties of the NET_{large} and the NET_{small} must be considered in the connecting process. The detailed considerations are as follows.

Connecting large-scale pore with small-scale pore. First of all, the added connecting throat is the small-scale throat, which should be correlated with the NET_{small}. Except for the throat length, the geometric properties of the added small-scale throat are determined based on the average values of throats in the NET_{small}. The length of the added small-scale throat is determined as follows. For two pores p_1 and p_2 with inscribed radii r_1 and r_2, the distance $d_t(p_1,p_2)$ is defined as

$$d_t(p_1,p_2) = d_e(p_1,p_2) - r_1 - r_2 \tag{3}$$

where $d_e(p_1,p_2)$ is the Euclidean distance between the two pore centers. If the two pores are connected by a throat, $d_t(p_1,p_2)$ is the length of this throat. The length of the added small-scale throat should be less than or equal to the maximum length $\widetilde{d}_t$ of throats in the NET_{small}. Each large-scale pore $p_{LPP,i}(i = 1, 2, \ldots, N_{LPP})$ of the NET_{large} can only connect its nearby pore $p_{SP,ii}(ii = 1, 2, \ldots, N_{SP,i})$ of the NET_{small} whose $d_t(p_{LPP,i}, p_{SP,ii})$ is less than or equal to the $\widetilde{d}_t$, where N_{LPP} is the number of large-scale pores in the NET_{large}, and $N_{SP,i}$ is the number of pores of the NET_{small} that meet this condition.

Secondly, the number of pores in the NET_{small} that can be connected to a large-scale pore $p_{LPP,i}$ of the NET_{large} is also correlated to the density and connectivity of the NET_{small}, the coordination number and radius of $p_{LPP,i}$ in the NET_{large}, and the radii of throats connected to $p_{LPP,i}$ in the NET_{large}. We use a parameter γ_S proposed by Jiang et al. (2013) to represent the density and connectivity of the NET_{small} as follows. Taking the center c_S of the NET_{small} as sphere center, we insert ξ concentric spheres of radii $0 < R_1 < R_2 < \ldots < R_\xi$ in the NET_{small}, and ensure that the largest sphere is within the NET_{small}. For the k-th ($k = 1, 2, \ldots, \xi$) concentric sphere, the number $N_{ST,k}$ of throats that penetrate the sphere is calculated by

$$N_{ST,k} = Card\left(\left\{t_{ST,j} \middle| d_e\left(c_S, p_{SP,j1}\right) < R_k < d_e\left(c_S, p_{SP,j2}\right), j = 1, 2, \cdots, N_{ST}\right\}\right) \tag{4}$$

where $Card()$ is a mathematical symbol, which is named cardinal number and indicates the number of elements in a set. It is implemented by traversing every throat in the NET_{small} one by one and calculating the number of throats that satisfy the conditions in the Eq. (4). $t_{ST,j}$ is the j-th throat in the NET_{small}, and N_{ST} is the number of throats in the NET_{small}; $p_{SP,j1}$ and $p_{SP,j2}$ are two pores connected by the throat $t_{ST,j}$. The parameter γ_S is defined as

$$\gamma_S = \frac{1}{\xi}\sum_{k=1}^{\xi}\frac{N_{ST,k}}{a_k} \tag{5}$$

where a_k is the surface area of the k-th concentric sphere. For more details, refer to Jiang et al. (2013).

The coordination number and radius of $p_{LPP,i}$ in the NET_{large} and the radii of throats connected to $p_{LPP,i}$ in the NET_{large} are represented as follows. For a $p_{LPP,i}$ of radius $r_{LPP,i}$ and coordination number $CN_{LPP,i}$ in

the NET_{large}, the area $a_{LPT,ij}$ of spherical crown occupied by the throat $t_{LPT,ij}$ is calculated by

$$a_{LPT,ij} = 2\pi r_{LPP,i}\left(r_{LPP,i} - \sqrt{r_{LPP,i}^2 - r_{LPT,ij}^2}\right) \tag{6}$$

where $r_{LPT,ij}$ is the radius of the throat $t_{LPT,ij}$, as shown in Fig. 3. The remaining surface area $sa_{LPP,i}$ of $p_{LPP,i}$ that are not occupied by throats is thus calculated by

$$sa_{LPP,i} = 4\pi r_{LPP,i}^2 - \sum_{j=1}^{CN_{LPP,i}} a_{LPT,ij} \tag{7}$$

Finally, the number $SCN_{LPP,i}$ of pores in the NET_{small} that can be connected to $p_{LPP,i}$ of the NET_{large} is calculated by

$$SCN_{LPP,i} = sa_{LPP,i}\gamma_S \tag{8}$$

Connecting fracture pore with small-scale pore. Since the fracture network is extremely dense (see Fig. 1c), if the scheme described above is used directly to connect fracture pores with small-scale pores, a small pore will be connected with a large number of fracture pores around it. In order to avoid this issue, we search for all the small-scale pores that can be connected to every fracture pore via using the Eq. (3) and the $\widetilde{d}_t$ (see the small-scale pores within the red shadow in Fig. 4). Each pore $p_{SP,i}$ of these small-scale pores is subsequently connected to one fracture pore p_{LFP} whose $d_t(p_{SP,i}, p_{LFP})$ is the smallest (see Fig. 4). Moreover, the length and geometric properties of the added small-scale throats are determined via the scheme described in Section 2.1.3.1.

Generation. The NET_{multi} is generated by following the process shown below.

1 For each large-scale pore $p_{LPP,i}$ of the NET_{large}, calculating the $SCN_{LPP,i}$ via using Eqs. (4)–(8). Finding its nearby pores of the NET_{small} that are possible to be connected with it, using the Eq. (3) and $\widetilde{d}_t$. Some obtained pores of the NET_{small} are connected to the pore $p_{LPP,i}$ using the added throats, according to the $SCN_{LPP,i}$ and the order of $d_t(p_{LPP,i}, p_{SP,ii})$ from small to large (see Fig. 4).

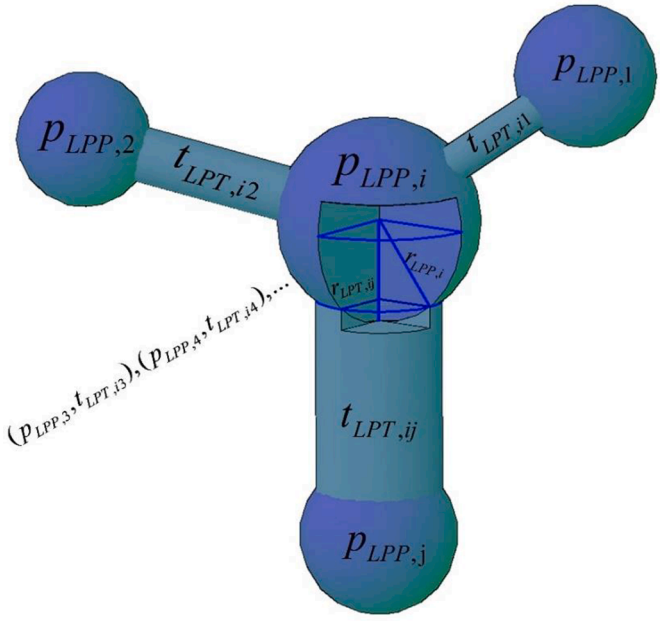

Fig. 3. A large-scale pore $p_{LPP,i}$ of radius $r_{LPP,i}$ is connected to j pores by j throats. The radius of jth throat is $r_{LPT,ij}$. Every throat occupies part of surface (spherical crown) of pore $p_{LPP,i}$.

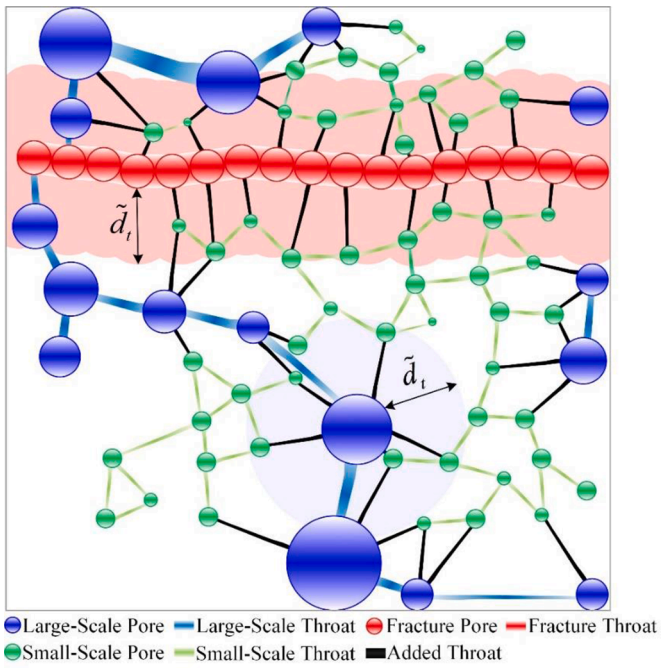

Fig. 4. The connections of small-scale pores (green) to large-scale pores (blue) and fracture pores (red) via the added throats (black). Small-scale pores within the bule shadow of thickness $\widetilde{d}_t$ are possible to be connected with the central large-scale pore. Each small-scale pore within the red shadow of thickness $\widetilde{d}_t$ is connected to the nearest fracture pore.

2 For all fracture pores of the NET_{large}, finding all the pores of the NET_{small} that can be connected to them by using the Eq. (3) and the $\widetilde{d}_t$. Every pore of the obtained small-scale pores is connected to the nearest fracture pores using a added throat (see Fig. 4).
3 Assigning the geometric properties to the added small-scale throats.
4 Through connecting small-scale pores with large-scale pores and fracture pores, the NET_{small} and the NET_{large} are integrated into a global connected pore network. We calculate the absolute permeability of the pore network and compare it to the experimental permeability. The calculation will be introduced later. If the match between them is poor, we will change the pore radius distribution and the throat radius distribution of micropores via resetting the types, mean values, and standard deviations of the distributions. Then, we regenerate the NET_{small} and reconstruct the global connected pore network to calculate its absolute permeability, until the calculation result is close to the experimental permeability (the relative error is less than 10%). The work flow is shown in Fig. 5.

Finally, the NET_{multi} is generated. Note that since the NET_{multi} is closely correlated with the NET_{large} and NET_{small}in terms of both geometry and topology, only three construction parameters are uncertain and need to be adjusted: the pore radius distribution and the throat radius distribution of the NET_{small} as well as f_S. The first two construction parameters are determined under the constraint of experimental permeability. The determination of f_S will be discussed later. Therefore, our method possesses significant conveniences.

2.2. Multiscale pore-fracture hybrid pore network calculation

The NET_{multi} has significant advantages in flow calculation, compared to the multiscale seepage model coupled with different methods. All void components in NET_{multi} are represented by the basic elements: pores and throats, which makes it possible to perform the global flow simulation via one solver. We extend the network simulator

developed by the professor Martin Blunt's group at Imperial College to simulate drainage in the NET_{multi}(Blunt et al., 2002; Valvatne and Blunt, 2004). Each iteration step of the network simulator includes two sub-steps: the displacement process and the flow flux solving process. The displacement process is based on the quasi-static model, that is, the flow velocity is assumed to be small enough so that the viscous force is negligible and the capillary force is control force. For more details of the displacement process, one can refer to the work of Valvatne and Blunt (2004). After the displacement process, all phase interfaces are updated at the boundaries between pores and throats. Therefore, it is possible to easily count the respective volumes of oil and water in all of pores and throats. The water saturation S_w is calculated as the ratio of water volume to the total volume of the NET_{multi}. Flow flux of a phase f can be solved by imposing the mass conservation equation at every pore, which is described as:

$$\sum_{j=1}^{n} q_{f,ij} = 0 \tag{9}$$

where n is the number of throats connected to the pore i, $q_{f,ij}$ is the flow flux of phase f in the throat ij connecting pore i and pore j. $q_{f,ij}$ can be written as:

$$q_{f,ij} = g_{f,ij}\left(P_{f,i} - P_{f,j}\right) \tag{10}$$

where $P_{f,i}$ and $P_{f,j}$ are the pressure of phase f in pore i and pore j, respectively; $g_{f,ij}$ is the hydraulic conductivity of phase f in throat ij. NET_{multi} contains large-scale pores and throats and small-scale pores and throats as well as fracture pores and throats. For the large-scale pores and throats, because its size is much larger than liquid slip length, the Knudsen number is small and the liquid slip effect can generally be ignored. $g_{f,ij}$ is written as (Valvatne and Blunt, 2004):

$$g_{f,ij} = \begin{cases} \dfrac{0.6A_{ij}^2 G_{ij}}{\mu_f l_{ij}} & 0 < G_{ij} \le 0.0481 \\ \dfrac{0.5623A_{ij}^2 G_{ij}}{\mu_f l_{ij}} & 0.0481 < G_{ij} \le 0.0625 \\ \dfrac{0.5A_{ij}^2 G_{ij}}{\mu_f l_{ij}} & 0.0625 < G_{ij} \le 0.0796 \end{cases} \tag{11}$$

where A_{ij} and l_{ij} are the cross sectional area and length of throat ij, respectively; G_{ij} is the shape factor of cross section of throat ij, $0 < G_{ij} \le 0.0481$ represents the cross section is triangular in shape, $0.0481 < G_{ij} \le 0.0625$ represents the cross section is quadrilateral in shape, $0.0625 < G_{ij} \le 0.0796$ represents the cross section is circular in shape; μ_f is the viscosity of phase f.

For the small-scale pores and throats, since the liquid slip length is comparable to its size, the Knudsen number is large and the liquid slip effect must be considered in $g_{f,ij}$ as (Afsharpoor and Javadpour, 2016; Ji et al., 2021):

$$g_{f,ij} = \begin{cases} \dfrac{\left(-0.012 + 0.057Ld_{ij} + 2G_{ij} - 0.0052Ld_{ij}^2 - 38G_{ij}^2 + 3.2Ld_{ij}G_{ij}\right)A_{ij}^2}{\mu_f l_{ij}} & G_{ij} < 0.04 \\ \dfrac{\left(-0.16 + 0.16Ld_{ij} + 6.4G_{ij} - 0.0055Ld_{ij}^2 - 50G_{ij}^2 + 1.7Ld_{ij}G_{ij}\right)A_{ij}^2}{\mu_f l_{ij}} & G_{ij} \ge 0.04 \end{cases} \tag{12}$$

where Ld_{ij} is the dimensionless slip length of liquid flow in throat ij, calculated by $Ld_{ij} = Ls_{ij}/\sqrt{A_{ij}}$, Ls_{ij} is the physical slip length of liquid flow in throat ij.

For the fracture pores and throats, $g_{f,ij}$ is adjusted as (Pruess and Tsang, 1990; Ebrahimi et al., 2014; Jiang et al., 2017a):

$$g_{f,ij} = \frac{w_{F,ij}h_{F,ij}^3}{12\mu_f l_{F,ij}} \tag{13}$$

where $w_{F,ij}$, $h_{F,ij}$, and $l_{F,ij}$ are the width, equivalent aperture, and length of fracture throat $t_{LFT,ij}$ connecting two fracture pores $p_{LFP,i}$ and $p_{LFP,j}$, respectively.

The linear equations of mass conservation of all the pores in the NET_{multi} can be obtained by formulas (9)~(13). Then, the linear equation system is solved using Gauss-Seidel method to obtain the convergent stable pressure field, according to the pressure boundary conditions (the inlet pressure $P_{in,t}$ of NET_{multi} and the outlet pressure P_{out} of NET_{multi}) in the current iteration step of drainage calculation. The subscript t of $P_{in,t}$ represents the current iteration step is the t-th iteration step in drainage computation.

The total flow flux $Q_{f,in}$ of phase f at the inlet interface of NET_{multi} is obtained by calculating the flow flux of each inlet pore in NET_{multi}:

$$Q_{f,in} = \sum_{k=1}^{n_{ib}} Q_{f,k} = \sum_{k=1}^{n_{ib}} \sum_{j=1}^{m} g_{f,kj}\left(P_{f,k} - P_{f,j}\right) \tag{14}$$

where n_{ib} is the number of inlet pores of NET_{multi}; $Q_{f,k}$ is the flow flux of phase f in the inlet pore k; m is the number of throats connected to the inlet pore k; $P_{f,k}$ and $P_{f,j}$ are the pressure of pore k and pore j in the stable pressure filed, respectively. Similarly, the total flow flux $Q_{f,out}$ of phase f at the outlet interface of NET_{multi} can be calculated. The absolute permeability K_{mf} of phase $f$at the t-th iteration step of drainage simulation can be calculated as:

$$K_{mf} = \frac{\mu_f Q_f L}{A\left(P_{in,t} - P_{out}\right)} \tag{15}$$

where $Q_f = \left(Q_{f,in} + Q_{f,out}\right)/2$; L is the vertical distance between the inlet interface and the outlet interface of NET_{multi}; A is the area of the inlet interface of NET_{multi}. Through the above computation process, the absolute permeability K_{sf} of phase f under the single-phase flow can be calculated based on the same pressure boundary conditions. The relative permeability K_{rf} of phase f at the t-th iteration step of drainage simulation is calculated by:

$$K_{rf} = \frac{K_{mf}}{K_{sf}} \tag{16}$$

In addition, the capillary pressure P_c at the t-th iteration step of drainage simulation is calculated by:

$$P_c = P_{in,t} - P_{out} \tag{17}$$

Throughout the drainage simulation, we slowly increase the inlet pressure and keep the outlet pressure constant. Each pressure point corresponds to an iteration step, in which the displacement process and the flow flux solving process are performed. Finally, the water saturation-capillary pressure curve and water saturation-relative permeability curve can be obtained.

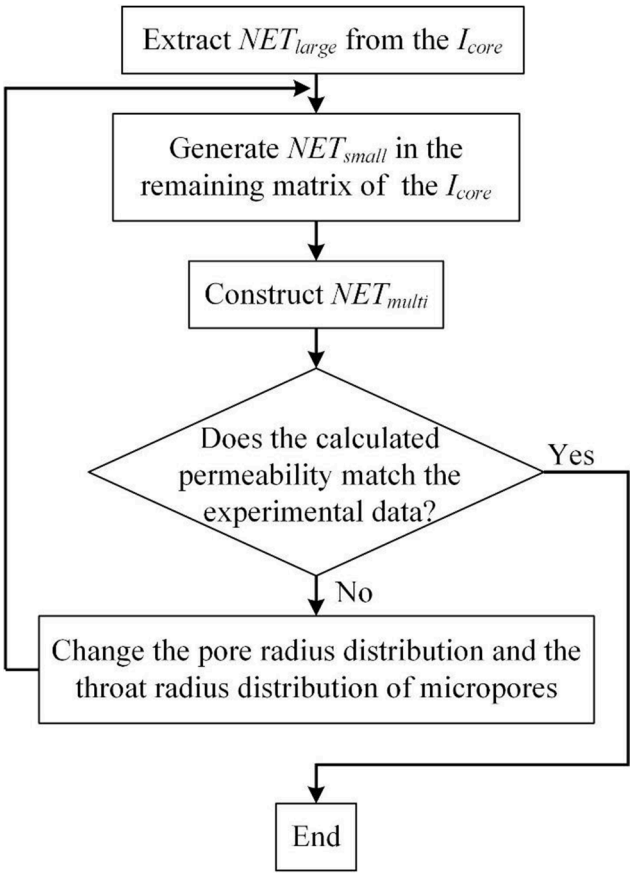

Fig. 5. Workflow of the multiscale pore-fracture hybrid pore network construction.

3. Results and discussion

To provide an insight into the multiscale pore-fracture hybrid pore network model and assess the model quality, two reservoir tight carbonate rocks from Ordovician formation in China, denoted as Ordos tight carbonate and Tarim tight carbonate, are used to generate multiscale hybrid pore networks.

3.1. Ordos tight carbonate

3.1.1. Pore-fracture hybrid pore network

The μCT image of the Ordos tight carbonate rock, along with its extracted pore-fracture hybrid pore network, is shown in Fig. 6. The voxel numbers of the μCT image are 1008 × 1008 × 1008, and the voxel size is 13.98 μm. The white and gray are matrix, which is mainly composed of quartz and clay minerals. The black represents voids, which comprise pore spaces and two fractures. In the extracted pore-fracture hybrid pore network, two curved fractures (red) are clearly revealed. The major properties, including absolute permeability, of the hybrid pore network are shown in Table 1. We note that the numbers of fracture pores and fracture throats are greater than those of large-scale pores and large-scale throats because fractures are represented by the dense pore networks. As the entire void space in μCT image has no overall connectivity in X- and Y-directions, the extracted hybrid pore network is not percolating in these two directions. The hybrid pore network has large permeability (Kz_L) of 752.57mD in Z-direction due to the perforative fracture in this direction (the left fracture in Fig. 6a and b). In order to evaluate the hybrid pore network, the Z-direction permeability (Kz_{LBM}) of the corresponding binary image is directly calculated using the two-relaxation-time Lattice Boltzmann model (TRT-LBM) (Pan et al., 2006), as shown in Table 1. The relative error between Kz_L and Kz_{LBM} is 8.68%, which is reasonable. The possible reason for this result is that the simplification of pore-fracture connecting spaces, which results in more flow probability. The good agreement between Kz_L and Kz_{LBM} indicates that the pore-fracture hybrid pore network extracted by the improved AB-MS algorithm is equivalent to the actual pore-fracture spaces. This lays a good foundation for the multiscale hybrid pore network generation.

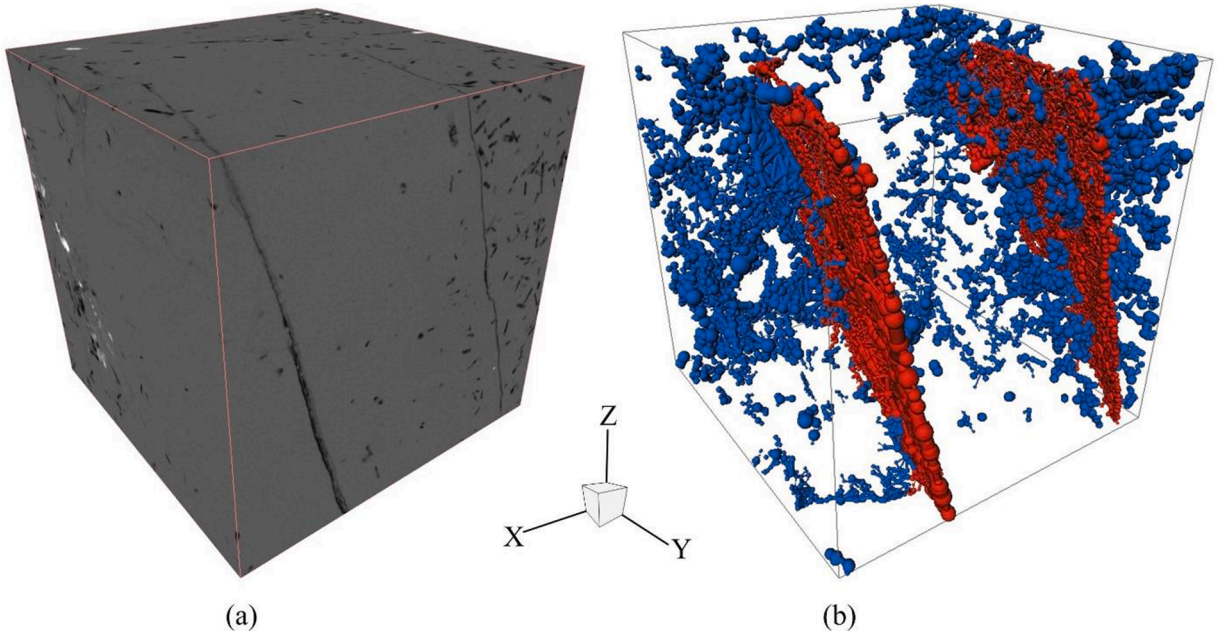

Fig. 6. (a) The μCT image of the Ordos tight carbonate rock. The voxel numbers are 1008 × 1008 × 1008, and the voxel size is 13.98 μm. The white and gray indicate matrix, and the black indicates voids. (b) Pore-fracture hybrid pore network extracted from the voids. Fracture pores and fracture throats are shown in red, and large-scale pores and large-scale throats are shown in blue.

Table 1
Properties of hybrid pore network and the absolute permeability calculated from our hybrid pore network and Lattice-Boltzmann model, respectively.

Property	N_{LPP}	N_{LPT}	N_{LFP}	N_{LFT}	N_{LP}	N_{LT}	ACN_L	Kz_L (mD)	Kz_{LBM} (mD)
Value	8630	12,680	27,912	56,227	36,542	68,907	3.77	752.57	687.22

$N_{LPP}$and N_{LPT} are the number of large-scale pores and large-scale throats, respectively. N_{LFP} and N_{LFT} are the numbers of fracture pores and fracture throats, respectively. N_{LP} and N_{LT} are the numbers of pores and throats in the hybrid pore network, respectively, $N_{LP} = N_{LPP} + N_{LFP}$ and $N_{LT} = N_{LPT} + N_{LFT}$. ACN_L is the average coordination number of the hybrid pore network. Kz_L and Kz_{LBM} are the absolute permeability in Z-direction, calculated from our hybrid pore network and Lattice-Boltzmann model, respectively.

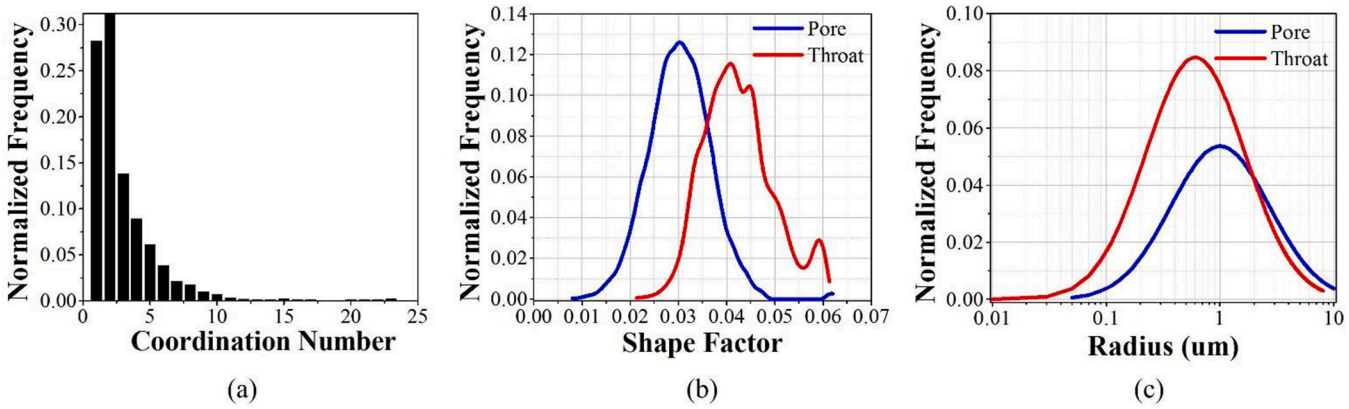

Fig. 7. Distributions of small-scale stochastic pore network parameters. The normalized (a) coordination number distribution and (b) shape factor distributions obtained from large-scale pores and throats of the extracted hybrid pore network (blue in Fig. 6b). (c) The distributions of pore radius and throat radius that are assumed to be lognormal with fixed mean values of 1 μm and 0.5 μm, respectively.

3.1.2. Multiscale pore-fracture hybrid pore network

The normalized coordination number distribution, pore shape factor distribution and throat shape factor distribution of large-scale pores and throats of the extracted hybrid pore network (see blue in Fig. 6b) is used for generating the small-scale stochastic pore network, as shown in Fig. 7a and b. It can be seen that the peak value and the average value of the coordination number distribution are 2 and 2.91, respectively. The peak values of the pore shape factor distribution and the throat shape factor distribution are about 0.0301 and 0.0413, indicating that the cross sections of large-scale pore spaces are mainly triangular in shape. Moreover, the distributions of pore radius and throat radius of small-scale stochastic pore network are assumed to be lognormal (see Fig. 7c) to study the effect of f_S first. The small-scale mean pore radius and mean throat radius are assumed to be 1 μm and 0.5 μm, respectively.

As mentioned in Section 2.1.3.3, only three construction parameters in the NET_{multi} are uncertain and need to be adjusted, in which the first two construction parameters are determined under the constraint of experimental permeability. Here, the effects of the third construction parameter f_S on the NET_{multi} and its single-phase and two-phase flow properties are investigated.

Different f_Ss are considered and the corresponding multiscale hybrid pore networks are constructed. Some properties of these networks are summarized in Table 2. As it can be seen, multiscale hybrid pore networks have higher average coordination number due to the presence of small-scale pores connected to adjacent large-scale pores and fracture pores. The average coordination numbers of the two multiscale hybrid pore networks with $f_S = 0.4$ and $f_S = 0.6$ are almost the same and did not increase with the increase of f_S. To clarify this situation, Fig. 8a shows the detailed average coordination number-f_S curve and Fig. 8b shows the coordination number distributions of three multiscale hybrid pore networks with $f_S = 0.4$, $f_S = 0.5$, and $f_S = 0.6$. It can be seen that the average coordination number tends to become almost constant with the increase of f_S, in this case about $f_S > 0.3$. The coordination number distributions of the three f_Ss agree well (see Fig. 8b). It indicates that the proposed method can ensure the constructed network is correlated in terms of geometry and topology and will not endlessly connect small-scale pores to adjacent large-scale pores and fracture pores. Two multiscale hybrid pore networks with different f_Ss are visualized in Fig. 9.

Table 2
Properties of multiscale hybrid pore networks constructed with various f_S.

f_S	0.05	0.1	0.2	0.4	0.6
N_{MP}	38,312	40,083	43,623	50,705	57,783
N_{MT}	77,965	98,604	130,561	172,904	197,628
ACN_M	4.07	4.92	5.99	6.82	6.84

$N_{MP}$and N_{MT} are the numbers of pores and throats in the multiscale hybrid pore network, respectively. ACN_M is the average coordination number of the multiscale hybrid pore network.

The absolute permeabilities of multiscale hybrid pore networks with different f_Ss are calculated in the X- Y- and Z-directions. The results are shown in Fig. 10. As can be seen, for the well-connected Z-direction of the extracted pore-fracture hybrid pore network, the integrated small-scale pore networks only enhance its permeability very little. The perforative fracture is the main flow channels in Z-direction (see Fig. 9). For the impermeable X- and Y-directions of the extracted pore-fracture hybrid pore network, the integrated small-scale pore networks significantly enhance permeability because small-scale pores connect large-scale pores and fracture pores to form the main flow paths. In this scenario, the permeability increases with the increase of f_S, but it becomes almost constant when $f_S > 0.3$ approximately. This effect of f_S on X- and Y- permeability is virtually the same as its effect on the model connectivity.

The drainage capillary-pressure saturation curves and relative permeabilities of multiscale hybrid pore networks with different f_Ss are also calculated in the X- Y- and Z-directions. Fig. 11 shows the capillary-pressure saturation curves. As can be seen, the residual water saturation decreases as the f_S increases, which can be due to the fact that the connections of small-scale pores with large-scale pores and fracture pores provide more escape routes for the trapped phase inside large-scale pore spaces. Another interesting observation is that the residual water saturation is almost constant for $f_S > 0.3$. This is consistent with the earlier observations that the connectivity and the absolute

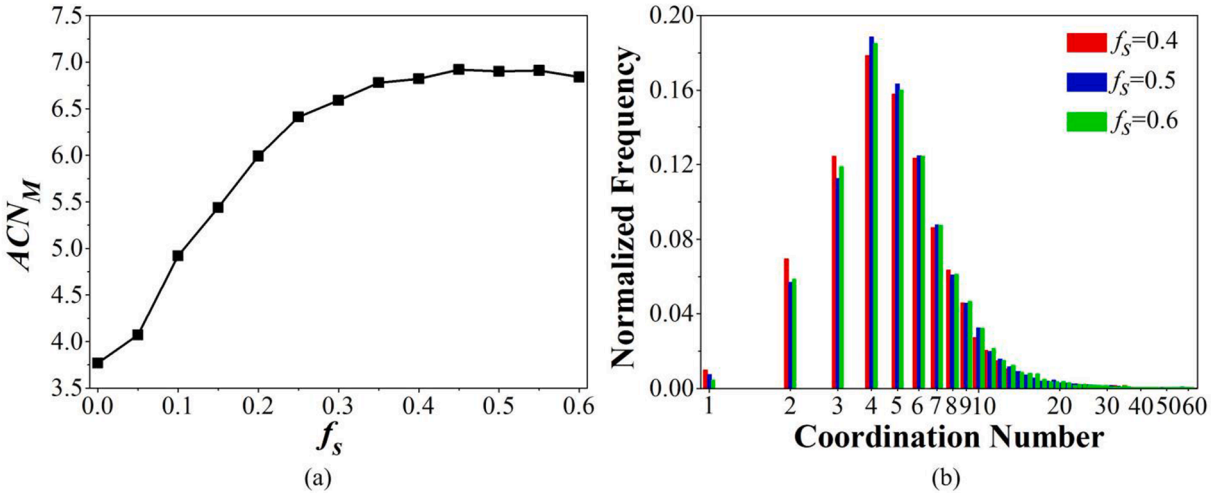

Fig. 8. (a) $ACN_M - f_S$ curve, where ACN_M is the average coordination number of the multiscale hybrid pore network. (b) The coordination number distributions of three multiscale hybrid pore networks with $f_S = 0.4$, $f_S = 0.5$, and $f_S = 0.6$.

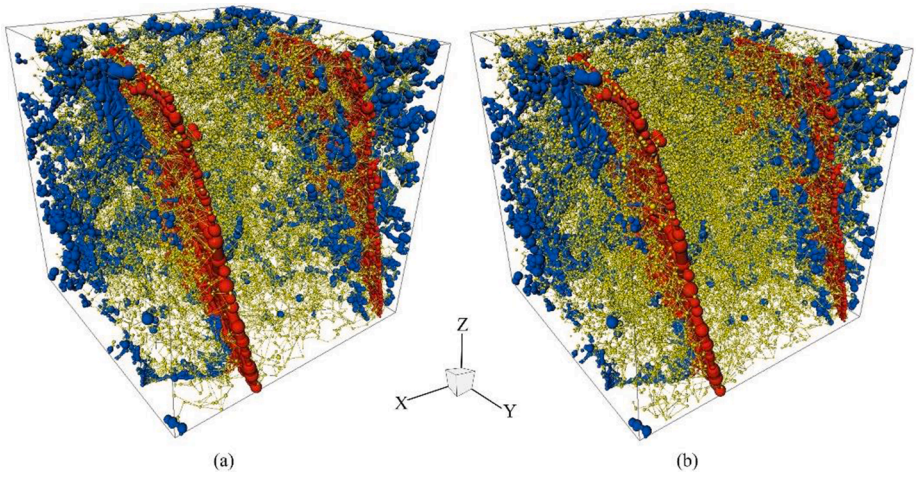

Fig. 9. Multiscale hybrid pore networks with different f_Ss. (a) $f_S = 0.4$, (b) $f_S = 0.6$. Small-scale pores and small-scale throats are shown in green.

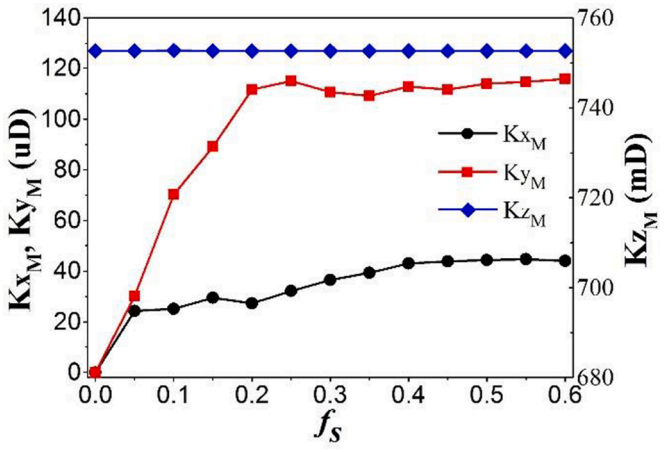

Fig. 10. The effects of f_S on absolute permeability of multiscale hybrid pore networks. Kx_M, Ky_M, and Kz_M are the absolute permeability in X-, Y-, and Z-directions, respectively. The unit of the left ordinate is μD and the unit of the right ordinate is mD.

permeability of the multiscale hybrid pore network hardly increases once $f_S > 0.3$. The curves for different f_Ss show good agreement when the water saturation is relatively large. The curves for X- and Z-directions (see Fig. 11a and c) have two percolation plateaus, although the right percolation plateau exhibits a tilt due to the slight increase of capillary-pressure. While the curves for Y-direction have only one percolation plateau (see Fig. 11b). To provide more insight into the displacement processes and clarify the differences, three moments St1, St2, and St3 in the displacement processes are selected (see Fig. 11) and the corresponding two-phase distributions are visualized in the network with $f_S = 0.4$, as shown in Fig. 12.

As can be seen from Fig. 12X-St1, the non-wetting phase (oil) invaded the right fracture and some pores adjacent to the fracture, resulting in the right percolation plateau in Fig. 11a. The non-wetting phase subsequently flowed through some paths between the two fractures and invaded the left fracture (see Fig. 12X-St2), with the rapid increase in pressure. The pressure jump between X-St1 and X-St2 in Fig. 11a corresponds to this process. The left fracture and some pores around it are rapidly occupied by the non-wetting phase (see Fig. 12X-St3), resulting in the left percolation plateau in Fig. 11a. With the further increase in pressure, the small-scale pores not occupied by non-wetting phase (see Fig. 12X-St3) are also invaded, which corresponds to the pressure jump after X-St3 in Fig. 11a. The displacement in Y-direction is

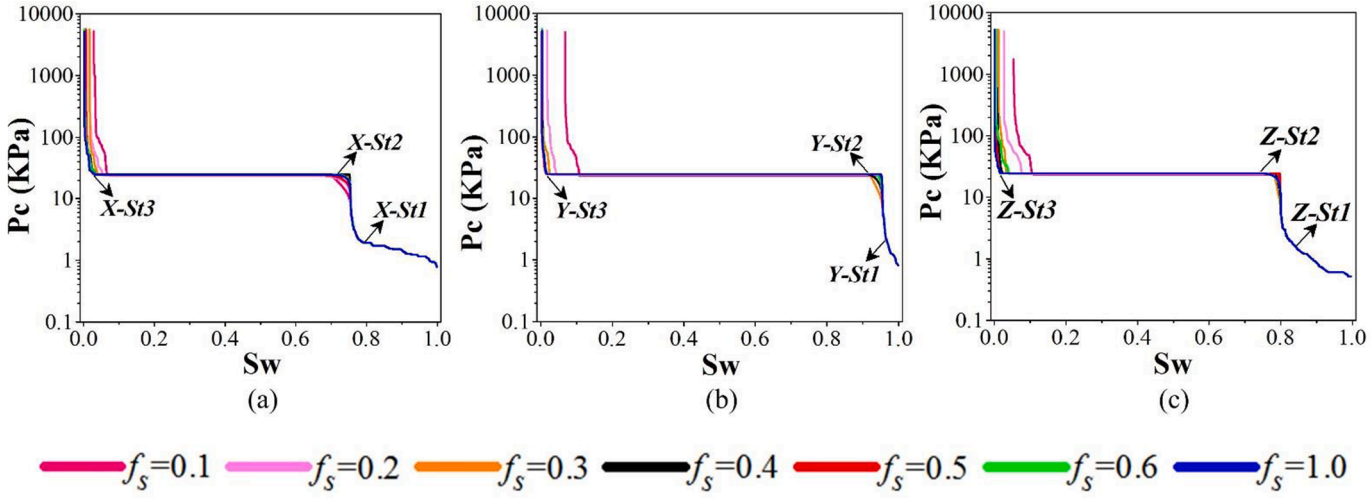

Fig. 11. The drainage capillary-pressure saturation curves in (a) X-direction, (b) Y-direction, and (c) Z-direction of multiscale hybrid pore networks with different f_Ss. St1, St2, and St3 are the three moments in the displacement processes.

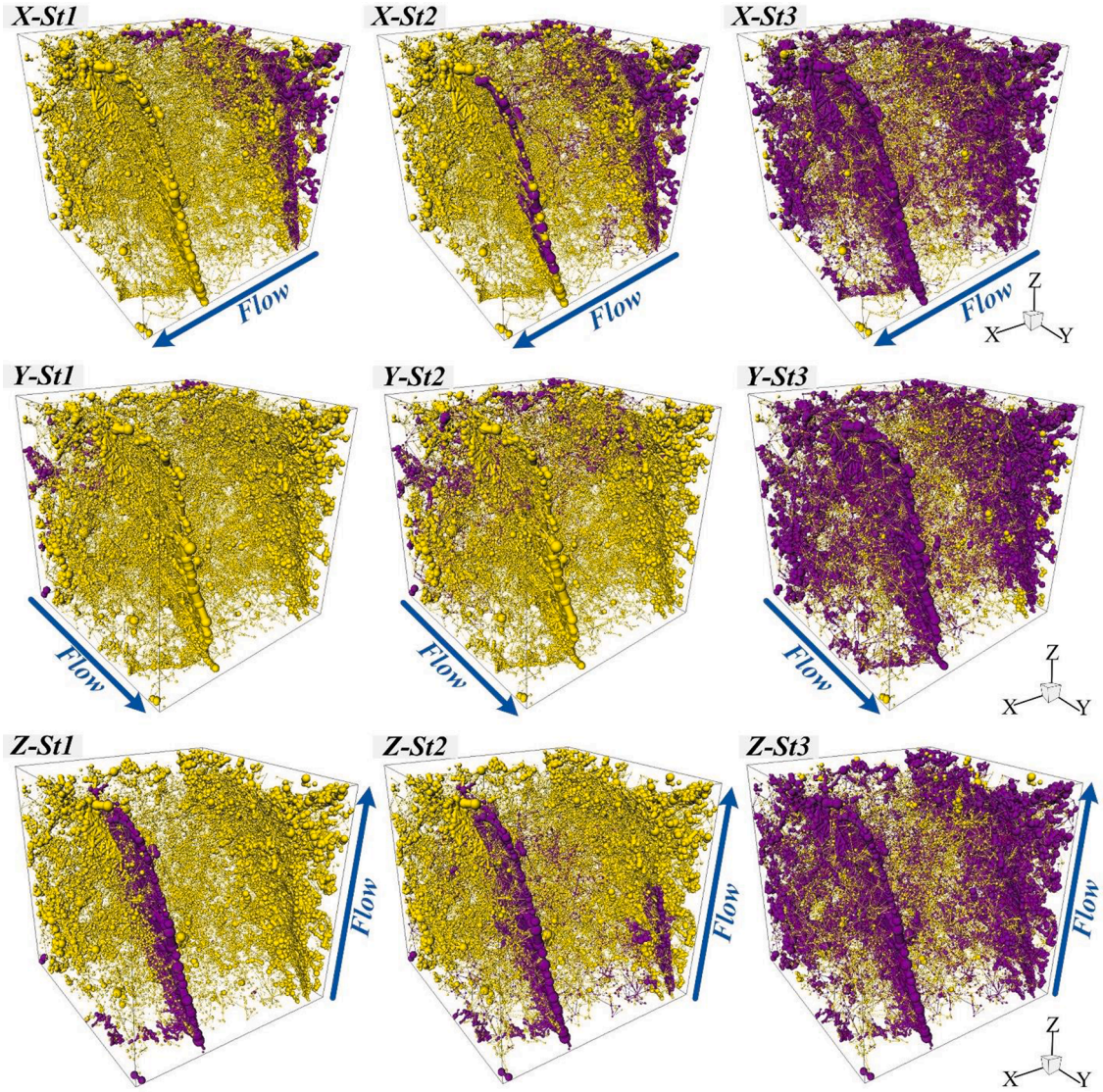

Fig. 12. The two-phase distributions in the multiscale hybrid pore networks with f_S = 0.4. X-St1, X-St2, and X-St3 are the three moments in the X-direction displacement (Fig. 11a). Y-St1, Y-St2, and Y-St3 are the three moments in the Y-direction displacement (Fig. 11b). Z-St1, Z-St2, and Z-St3 are the three moments in the Z-direction displacement (Fig. 11c). Wetting phase (water) is shown in yellow and non-wetting phase (oil) is shown in purple.

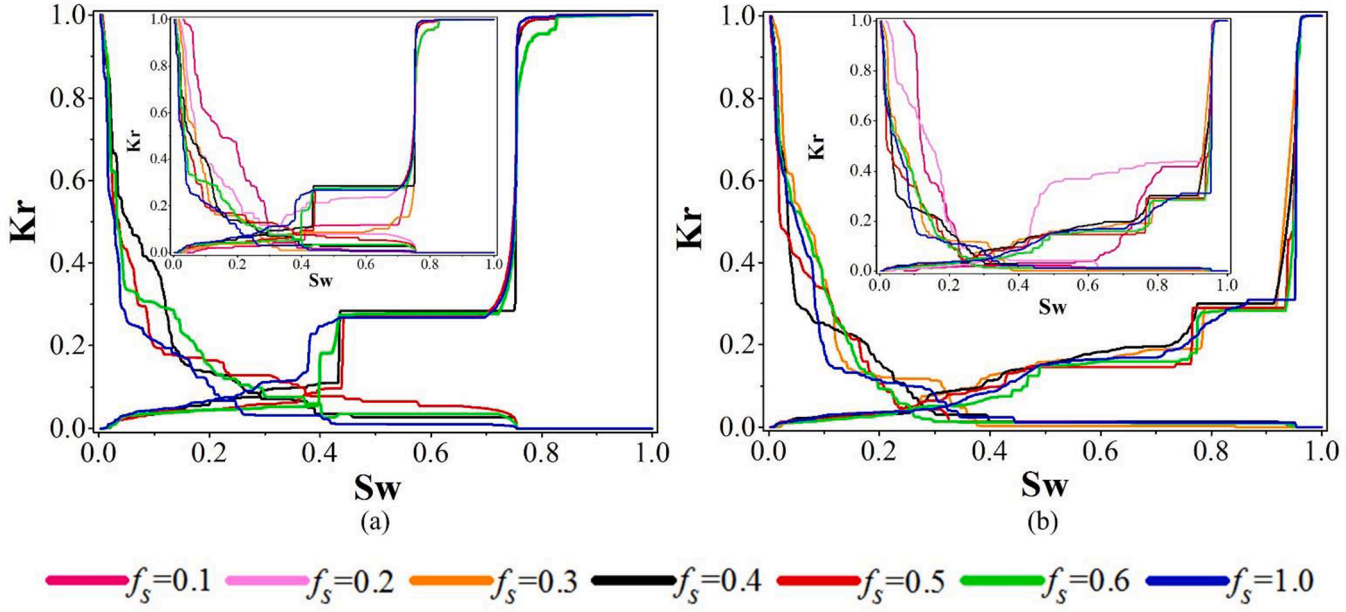

Fig. 13. The relative permeability curves in (a) X-direction and (b) Y-direction of multiscale hybrid pore networks with different f_Ss.

visualized in Fig. 12Y-St1, 12Y-St2, and 12Y-St3. Since the two fractures did not penetrate in Y-direction, the non-wetting phase first invaded some small-scale pores and throats (see Fig. 12Y-St1), with the rapid increase in pressure. The pressure jump between Y-St1 and Y-St2 in Fig. 11b corresponds to this process. Then, the two fractures were invaded by the non-wetting phase almost at the same time (see Fig. 12Y-St2 and Y-St3). Hence, the curves in Fig. 11b have only one larger percolation plateau. Fig. 12Z-St1, 12Z-St2, and 12Z-St3 show the displacement in Z-direction. Since the right fracture does not penetrate in this direction, the curves (see Fig. 11c) also have two percolation plateaus. It should be noted that the right fracture was invaded in two ways: the nonwetting phase from the left fracture and the nonwetting phase from the inlet (see Fig. 12Z-St2).

Fig. 13 shows the relative permeability curves in X- and Y-directions. The effect of f_S on the relative permeability is large. As can be seen from the subgraph in Fig. 13a, the relative permeability curves in X-direction show large variability when f_S is little (0.1, 0.2, 0.3), but they converge to an almost constant curve at $f_S \geq 0.4$ (see Fig. 13a). The relative permeability curves in Y-direction settle to a constant curve at $f_S \geq 0.3$ (see Fig. 13b). The small variability between convergent curves may be related to the fact that the flow paths become more tortuous with the increase of small-scale pores.

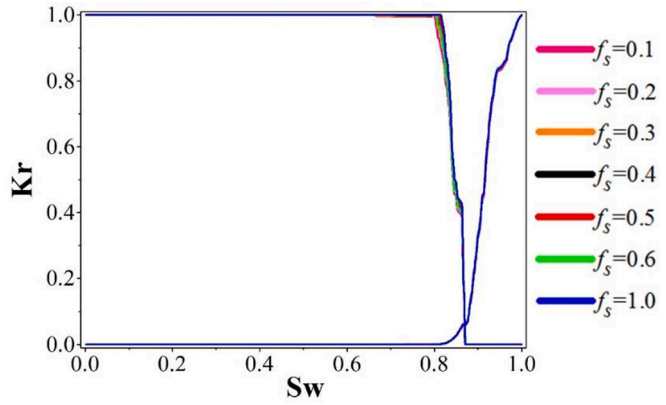

Fig. 14. The relative permeability curves in Z-direction of multiscale hybrid pore networks with different f_Ss.

Fig. 14 shows the relative permeability curves in Z-direction. The effect of f_S on the relative permeability is little because the perforative fracture in Z-direction provides the main flow path (see Fig. 12Z-St1). Although the processes of water saturation change in the X- Y- and Z-directions are similar (see Fig. 11), the water relative permeability in Z-direction rapidly decreases to the minimum and the oil relative permeability rapidly increases to the maximum due to the fluid channeling in the perforative fracture. The isotonic point of relative permeability shifts to the higher saturations (see Fig. 14). According to the results of absolute permeability (Fig. 10) and relative permeability (Fig. 13 and Fig. 14) in the three directions, it can be seen that there is a significant difference between the flow along the perforative fracture direction and the flow along other directions, which is one of the main feature of the heterogeneity of tight carbonate rocks.

The constructed multiscale hybrid pore network generally tends to have stable single-phase and two-phase flow results as well as robustness when $f_S \geq 0.4$. It means that these small-scale pore networks are sufficient to represent the properties of micropores. Moreover, a larger f_S will introduce excessive elements and lead to expensive computational demands, while a smaller f_S will result in inaccurate results without representativeness. Therefore, we set $f_S = 0.4$ to construct the NET_{multi} for taking into account both the calculation accuracy and the calculation efficiency in the study. Note that $f_S = 0.4$ is only used for this study, because the analysis of f_S is intended to be illustrative and provide more insight of the method rather than concluding the unique solution of f_S for various tight carbonates.

The experimental permeability of the Ordos tight carbonate rock in the Y-direction is 298.18μD. The distributions of pore radius and throat radius of small-scale stochastic pore network are re-determined under the constraint of experimental permeability, as shown in Fig. 15a. The distributions are lognormal. The small-scale mean pore radius and mean throat radius are 2 μm and 1 μm, which are larger than the earlier assumptions (see Fig. 7c). The calculated absolute permeability of multiscale hybrid pore network in Y-direction is 315.94μD, and the relative error between this result and the experimental data is 5.39%. Small changes of the small-scale radius distributions have a great influence on the permeability: jumping from 112.87μD (see Fig. 10) to 315.94μD. This is related to the fact that the connections of small-scale pores with large-scale pores and fracture pores provide the main flow paths. The calculated drainage capillary-pressure saturation curve is shown in Fig. 15b. The capillary-pressure saturation curve of $f_S = 0.4$ in Fig. 11b is

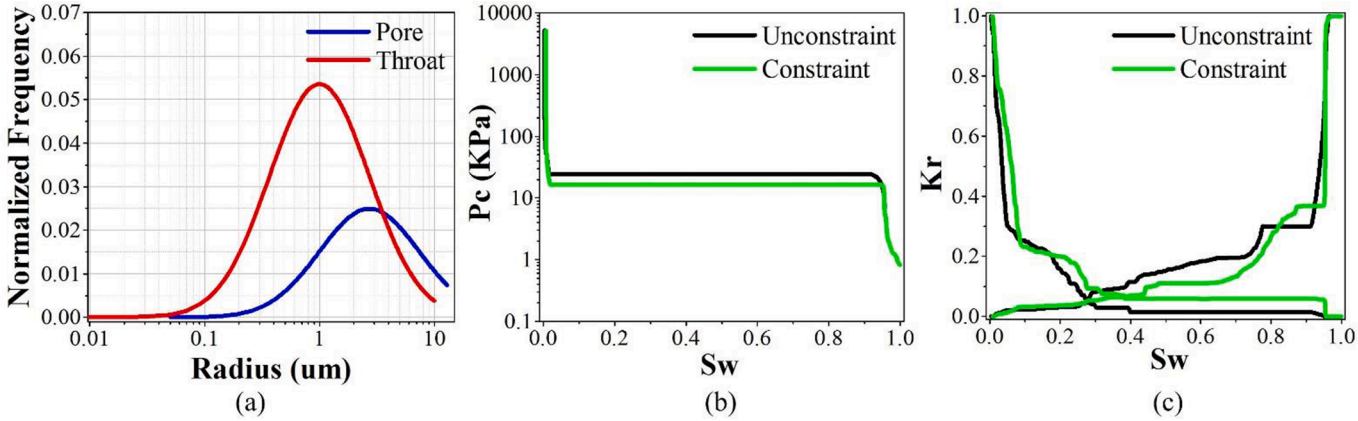

Fig. 15. (a) The distributions of pore radius and throat radius of small-scale stochastic pore network that are determined under the constraint of experimental permeability. The capillary-pressure saturation curves (b) and relative permeability curves (c). The unconstrained capillary-pressure saturation curve is obtained from Fig. 11b at $f_S = 0.4$. The unconstrained relative permeability curve is obtained from Fig. 13b at $f_S = 0.4$.

shown again in Fig. 15b for comparison. As expected, the pressure of percolation plateau of the constrained curve is lower. Fig. 15c shows the calculated drainage relative permeability curve and the unconstrained relative permeability curve of $f_S = 0.4$ (see Fig. 13b). As can be seen, the water relative permeability curve shifts down and the non-wetting phase (oil) relative permeability curve shifts up, as well as the isotonic point of relative permeability moves right to larger saturation, indicating that the displacement is more favorable. Since there is only experimental permeability in Y direction, we only discuss them in Y direction here. It is not possible to implement a direct comparison between the experimental results and the two-phase flow calculated results after constrained, but the work is currently in progress. The major contribution of this study is the multiscale pore-fracture hybrid pore network modeling method. Moreover, the drainage simulations in NET_{multi} were performed on a personal computer and the computational time was 3minutes, 29seconds, which was quite short for this tight carbonate with $14.09^3 mm^3$ sizes and multiscale pores-fractures. The presented model reduced the computational memory and improved the computational efficiency significantly and showed the potential for processing relatively large size tight carbonates on a personal computer.

3.2. Tarim tight carbonate

For this reservoir tight carbonate rock from Tarim Basin, we perform μCT experiment to acquire the scanning image, as shown in Fig. 16a. The resolution of the μCT experiment is also 13.98 μm. The voxel numbers of the μCT image are 722 × 1168 × 1139. The extracted pore-fracture hybrid pore network is shown in Fig. 16b. As can be seen, an irregular curved fracture (red) is clearly revealed. The basic properties of the extracted pore-fracture hybrid network are summarized in Table 3. The hybrid pore network is not percolating in Z-direction because the entire void space in μCT image has no global connected paths in this direction.

The normalized coordination number distribution, pore shape factor distribution and throat shape factor distribution of large-scale pores and throats of the extracted hybrid pore network (see blue in Fig. 16b) are obtained to generate small-scale stochastic pore network, as shown in Fig. 17a and b. As can be seen, the pore shape factor and throat shape factor are mostly less than 0.0481, indicating that their cross sectional shape is mainly triangle. The mean value of the coordination number distribution is 2.66. Then, the experimental permeability of the Tarim tight carbonate rock in the Z-direction is 739.33μD. The distributions of pore radius and throat radius of small-scale stochastic pore network are set to lognormal and determined under the constraint of experimental permeability, as shown in Fig. 17c. The small-scale mean pore radius and mean throat radius are 2 μm and 1 μm, respectively. The absolute permeability of multiscale hybrid pore network in Z-direction is calculated as 767.79μD, and the relative error between this result and the experimental result is 3.71%. The multiscale hybrid pore network is visualized in Fig. 16c, and major properties of the network are shown in Table 4. As can be seen, the absolute permeability of the multiscale

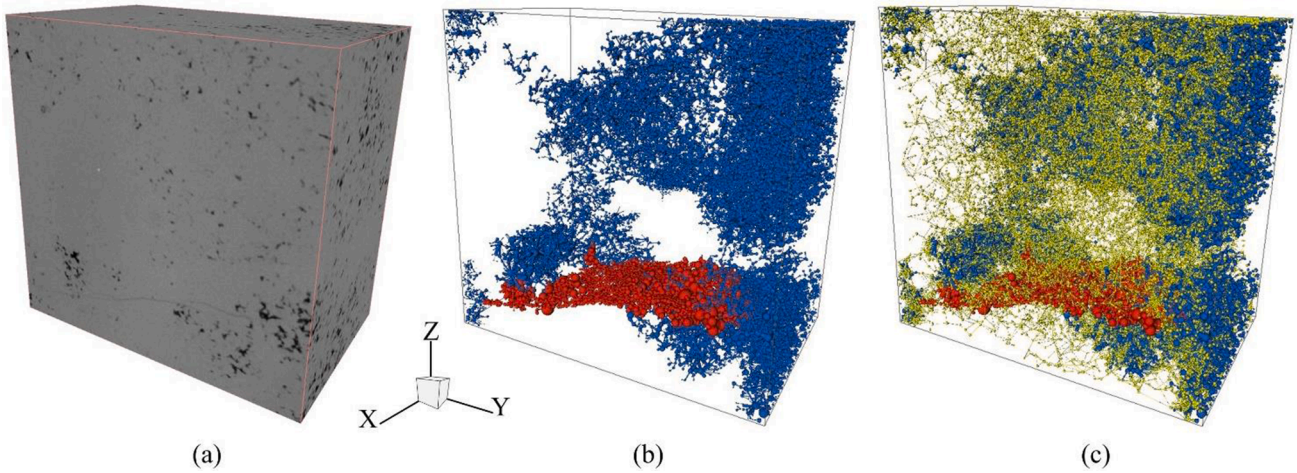

Fig. 16. (a) The μCT image of Tarim tight carbonate. The voxel numbers are 722 × 1168 × 1139, and the voxel size is 13.98 μm. (b) Pore-fracture hybrid pore network extracted from the void spaces of (a) μCT image. (c) Multiscale hybrid pore network with $f_S = 0.4$.

Table 3
Properties of the pore-fracture hybrid pore network.

Property	N_{LPP}	N_{LPT}	N_{LFP}	N_{LFT}	N_{LP}	N_{LT}	ACN_L	Kx_L (mD)	Ky_L (mD)
Value	23,132	30,826	13,386	26,838	36,518	57,664	3.16	1867.71	15.58

Kx_L and Ky_L are the absolute permeability of the pore-fracture hybrid pore network in X- and Y-directions.

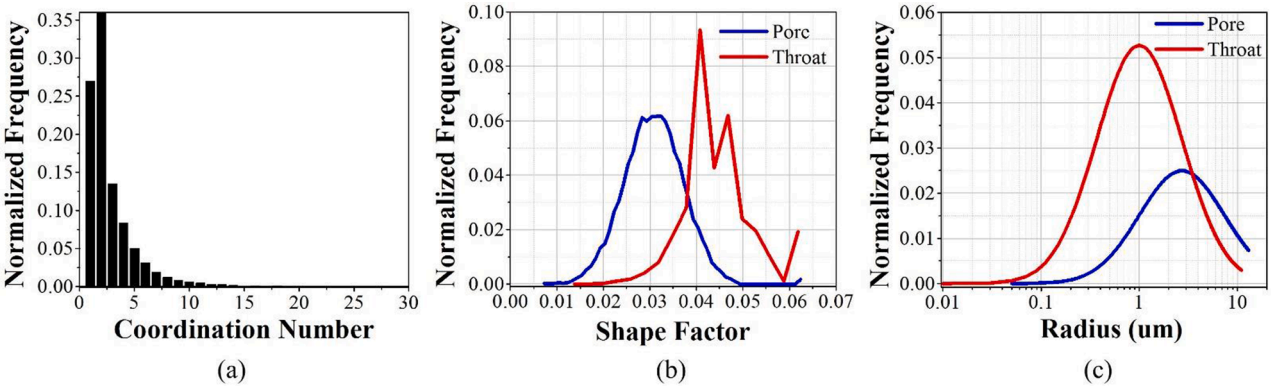

Fig. 17. Distributions of small-scale stochastic pore network parameters. The normalized (a) coordination number distribution and (b) shape factor distributions obtained from large-scale pores and throats of the extracted pore-fracture hybrid pore network (bule in Fig. 16b). (c) The distributions of pore radius and throat radius that are set to be lognormal and determined under the constraint of experimental permeability.

Table 4
Properties of multiscale hybrid pore network with $f_S = 0.4$.

Property	N_{MP}	N_{MT}	ACN_M	Kx_M (mD)	Ky_M (mD)	Kz_M (μD)
Value	50,042	172,394	6.89	1867.84	15.72	767.79

Kx_M, Ky_M and Kz_M are the absolute permeability of the multiscale hybrid pore network in X- Y- and Z-directions.

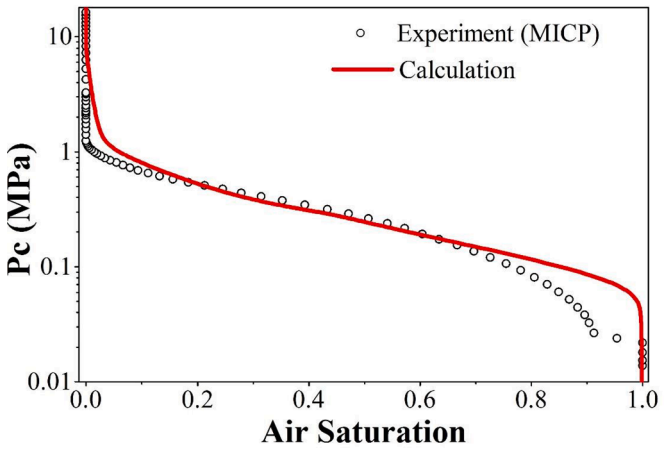

Fig. 18. Capillary-pressure saturation curve simulated in the multiscale hybrid pore network versus capillary-pressure saturation curve acquired by the mercury injection capillary pressure (MICP) experiment.

hybrid pore network in X- and Y- directions is almost the same as that of the pore-fracture hybrid pore network in the two directions (see Table 3), which is consistent with the earlier observation and Jiang et al.' study that the integrated small-scale pore network only leads to a very small increase in absolute permeability of the well-connected direction of the extracted large-scale network.

Fig. 18 shows the capillary-pressure saturation curve result simulated in the multiscale hybrid pore network and the mercury injection capillary pressure (MICP) experiment result of the Tarim tight carbonate rock. As can be seen, the simulated capillary-pressure saturation curve matches the experimental result well, though some of the detailed capillary-pressure behavior is not captured by the multiscale hybrid pore network. The simulated curve is slightly higher than the experimental result when the air saturation is low. The possible reason for this phenomenon is that the connectivity of small-scale pores is poorer than that of the actual micropores due to the strict space constraints on the small-scale throats, which makes mercury more difficult to enter. Moreover, the percolation plateau of the simulated curve exhibits a certain tilt because the fracture is small and does not dominate in the whole system.

4. Conclusions and outlook

In this study, a novel method is proposed to construct the multiscale pore-fracture hybrid pore network model for drainage in tight carbonate rocks. This model consists of nanometer pores, micron pores and fractures, and includes the flow characteristics in them. Firstly, considering the different flow characteristics in pore spaces and fractures, pores and fractures in a low-resolution μCT image are extracted by medial axis-maximal ball algorithm and medial surface algorithm, respectively, to generate a pore-fracture hybrid pore network. Subsequently, a statistics-based small-scale stochastic pore network is established in the μCT image solid domains to represent the micropores unresolved by the image. Then, the two pore networks are organically integrated into a multiscale hybrid pore network by the added small-scale throats under the constraint of experimental permeability. We extract a pore-fracture hybrid pore network from the μCT image of an Ordos tight carbonate rock and calculate the absolute permeability in the permeable Z-direction. The result is compared with that calculated by LBM. The relative error between them is 8.68% indicating that the pore-fracture hybrid pore network extracted by the developed AB-MS algorithm is physically realistic. The effects of the only uncertain construction parameters f_S on connectivity, single-phase and two-phase flow properties are further investigated. The multiscale hybrid pore network is robust and its coordination number distribution, absolute permeability and relative permeability curve tend to be convergent, when $f_S \geq 0.4$. These introduced small-scale pore networks are sufficient to represent the properties of micropores. Our proposed method can ensure the multiscale hybrid pore network is geometrically and topologically relevant besides will not endlessly connect small-scale pores to adjacent large-scale pores

and fracture pores. The effects of fractures on two-phase flow are also investigated. Incorporating fractures and micropores in the drainage model is important. Furthermore, we construct a multiscale pore-fracture hybrid pore network for a Tarim tight carbonate rock and calculate the capillary-pressure saturation curve. The multiscale hybrid pore network model is validated by comparing the calculated result with the mercury injection capillary pressure experiment data. The calculated capillary-pressure saturation curve matches the experimental data well.

It can be concluded that the proposed method can accurately, efficiently, conveniently construct multiscale pore-fracture hybrid pore network of tight carbonate rock for evaluating the drainage characteristics. The presented method is compatible with various sources of micropore parameters. We use some parameters (tortuosity, coordination number distribution, shape factor distribution) of large-scale pores and throats to represent the micropores, which is convenient and economic but may be somewhat sketchy for some applications. In future studies researchers can adopt our method and combine various sources of micropore parameters to further extend it as needed Eqs. (2), ((9)–(17)).

CRediT authorship contribution statement

Zhipeng Xu: Investigation, Conceptualization, Methodology, Validation, Writing – original draft, Writing – review & editing. **Mian Lin:** Investigation, Conceptualization, Writing – original draft, Writing – review & editing, Funding acquisition. **Lili Ji:** Conceptualization, Methodology, Writing – original draft, Writing – review & editing, Funding acquisition. **Wenbin Jiang:** Investigation, Validation, Writing – original draft, Writing – review & editing. **Gaohui Cao:** Validation, Writing – original draft, Writing – review & editing. **Leige Xu:** Writing – original draft, Writing – review & editing.

Declaration of Competing Interest

The authors declare that they have no known competing financial interests or personal relationships that could have appeared to influence the work reported in this paper.

Data availability

Data will be made available on request.

Acknowledgments

This work is supported by the National Natural Science Foundation of China (Grant No. 42030808), the National Natural Science Foundation of China (Grant No. 41690132), the Strategic Priority Research Program of the Chinese Academy of Sciences (Grant No. XDA14010304), the Major National Science and Technology Special Program of China (Grant No. 2017ZX05037-001), the National Natural Science Foundation of China (Grant No. 41574129). We thank Dr. G. Villarini and the anonymous reviewers for their constructive comments on this manuscript.

References

Afsharpoor, A., Javadpour, F., 2016. Liquid slip flow in a network of shale noncircular nanopores. Fuel 180, 580–590. https://doi.org/10.1016/j.fuel.2016.04.078.

Arns, C.H., Bauget, F., Limaye, A., Sakellariou, A., Senden, T.J., Sheooard, A.P., Sok, R. M., Pinczewski, W.V., Bakke, S., Berge, L.I., Øren, P.E., 2005. Pore-scale characterization of carbonates using X-ray microtomography. SPEJ Soc. Pet. Eng. J. 10 (04), 475–484. https://doi.org/10.2118/90368-PA.

Bauer, D., Youssef, S., Fleury, M., Bekri, S., Rosenberg, E., Vizika, O., 2012. Improving the estimations of petrophysical transport behavior of carbonate rocks using a dual pore network approach combined with computed microtomography. Transp. Porous Media 94, 505–524. https://doi.org/10.1007/s11242-012-9941-z.

Bultreys, T., Van Hoorebeke, L., Cnudde, V., 2015. Multi-scale, micro computed tomography-based pore network models to simulate drainage in heterogeneous rocks. Adv. Water Resour. 78, 36–49. https://doi.org/10.1016/j.advwatres.2015.02.003.

Blunt, M.J., Jackson, M.D., Piri, M., Valvatne, P.H., 2002. Detailed physics, predictive capabilities and macroscopic consequences for pore-network models of multiphase flow. Adv. Water Resour. 25 (8–12), 1069–1089. https://doi.org/10.1016/S0309-1708(02)00049-0.

Blunt, M.J., Bijeljic, B., Dong, H., Gharbi, O., Iglauer, S., Mostaghimi, P., Paluszny, A., Pentland, C., 2013. Pore-scale imaging and modelling. Adv. Water Resour. 51, 197–216. https://doi.org/10.1016/j.advwatres.2012.03.003.

Cao, G., Lin, M., Jiang, W., Li, H., Yi, Z., Wu, C., 2017. A 3D coupled model of organic matter and inorganic matrix for calculating the permeability of shale. Fuel 204, 129–143. https://doi.org/10.1016/j.fuel.2017.05.052.

Dong, H., Blunt, M.J., 2009. Pore-network extraction from micro-computerized-tomography images. Phys. Rev. E 80 (3), 036307. https://doi.org/10.1103/PhysRevE.80.036307.

Ebrahimi, A.N., Wittel, F.K., Araújo, N.A.M., Herrmann, H.J., 2014. Multi-scale approach to invasion percolation of rock fracture networks. J. Hydrol. 519, 353–363. https://doi.org/10.1016/j.jhydrol.2014.07.012.

Erzeybek, S., Akin, S., 2008. Pore network modeling of multiphase flow in fissured and vuggy carbonates. In: Proceedings of the SPE Symposium on Improved Oil Recovery. Society of Petroleum Engineers.

Gooya, R., Bruns, S., Müter, D., Moaddel, A., Harti, R.P., Stipp, S.L.S., Sørensen, H.O., 2016. Effect of tomography resolution on the calculated microscopic properties of porous materials: comparison of sandstone and carbonate rocks. Appl. Phys. Lett. 109 (10), 104102 https://doi.org/10.1063/1.4962389.

Hughes, R.G., Blunt, M.J., 2001. Network modeling of multiphase flow in fractures. Adv. Water Resour. 24, 409–421. https://doi.org/10.1016/S0309-1708(00)00064-6.

Idowu, N.A., Blunt, M.J., 2010. Pore-scale modelling of rate effects in waterflooding. Transp. Porous Media 83, 151–169. https://doi.org/10.1007/s11242-009-9468-0.

Ji, L., Lin, M., Jiang, W., Cao, G., Xu, Z., Hao, F., 2021. An improved rock typing method for tight sandstone based on new rock typing indexes and thee weighted fuzzy kNN algorithm. J. Petro. Sci. Eng. 210, 109956 https://doi.org/10.1016/j.petrol.2021.109956.

Jiang, W., Lin, M., Yi, Z., Li, H., Wu, S., 2017a. Parameter determination using 3D FIB-SEM images for development of effective model of shale gas flow in nanoscale pore clusters. Transp. Porous Media 117, 5–25. https://doi.org/10.1007/s11242-016-0817-5.

Jiang, Z., Wu, K., Couples, G., Van Dijke, M.I.J., Sorbie, K.S., Ma, J., 2007. Efficient extraction of networks from three-dimensional porous media. Water Resour. Res. 43, W12S03. https://doi.org/10.1029/2006WR005780.

Jiang, Z., van Dijke, M., Sorbie, K., Couples, G., 2013. Representation of multiscale heterogeneity via multiscale pore networks. Water Resour. Res. 49, 1–13. https://doi.org/10.1002/wrcr.20304, 2013.

Jiang, Z., Van Dijke, M.I.J., Geiger, S., Ma, J., Couples, G.D., Li, X., 2017b. Pore network extraction for fractured porous media. Adv. Water Resour. 107, 280–289. https://doi.org/10.1016/j.advwatres.2017.06.025.

Karpyn, Z.T., Piri, M., 2007. Prediction of fluid occupancy in fractures using network modeling and x-ray microtomography. I: data conditioning and model description. Phys. Rev. E 76, 016315. https://doi.org/10.1103/PhysRevE.76.016315.

Lee, T.C., Kashyap, R.L., Chu, C.N., 1994. Building skeleton models via 3-D medial surface/axis thinning algorithms. CVGIP Graph. Model Image Process. 56 (6), 462–478. https://doi.org/10.1006/cgip.1994.1042.

Li, Z.H., Yang, H.T., Sun, Z., Espinoza, D.N., Balhoff, M.T., 2021. A probability-based pore network model of particle jamming in porous media. Transp. Porous Media 139, 419–445. https://doi.org/10.1007/s11242-021-01673-4.

Lindquist, W., Lee, S., 1996. Meidal axis analysis of void structure in three-dimensional tomographic images of porous media. J. Geophys. Res. 101 (B4), 8297–8310. https://doi.org/10.1029/95JB03039.

Mehmani, A., Prodanović, M., 2014. The effect of microporosity on transport properties in porous media. Adv. Water Resour. 63, 104–119. https://doi.org/10.1016/j.advwatres.2013.10.009.

Müter, D., Pedersen, S., Sørensen, H.O., Feidenhans'l, R., Stipp, S.L.S., 2012. Improved segmentation of X-ray tomography data from porous rock using a dual filter approach. Comp. Geosci. 49, 131–139. https://doi.org/10.1016/j.cageo.2012.06.024.

Müter, D., Sørensen, H.O., Jha, D., Harti, R., Dalby, K.N., Suhnoen, H., Feidenhans'l, R., Engstrøm, F., Stipp, S.L.S., 2014. Resolution dependence of petrophysical parameters derived from X-ray tomography of chalk. Appl. Phys. Lett. 105 (4), 043108 https://doi.org/10.1063/1.4891965.

Prodanović, M., Mehmani, A., Sheppard, A.P., 2014. Imaged-based multiscale network modelling of microporosity in carbonates. Geol. Soc. London Spec. Publ. 406, SP406–SP409. https://doi.org/10.1144/SP406.9.

Silin, D.B., Jin, G.D., Patzek, T.W., 2003. Robust determination of the pore space morphology in sedimentary rocks. In: Proceedings of the SPE Annual Technical Conference and Exhibition. Society of Petroleum Engineers, Denver, Colo.

Pak, T., Butler, I.B., Geiger, S., van Dijke, M., Jiang, Z., Surmas, R., 2016. Multiscale pore-network representation of heterogeneous carbonate rocks. Water Resour. Res. 52, 5433–5441. https://doi.org/10.1002/2016WR018719.

Pan, C.X., Luo, L.S., Miller, C.T., 2006. An evaluation of lattice Boltzmann schemes for porous medium flow simulation. Comput. Fluids 35 (8), 898–909. https://doi.org/10.1016/j.compfluid.2005.03.008.

Pruess, K., Tsang, Y.W., 1990. On two-phase relative permeability and capillary pressure of rough-walled rock fractures. Water Resour. Res. 26 (9), 1915–1926. https://doi.org/10.1029/WR026i009p01915.

Rabbani, A., Jamshidi, S., Salehi, S., 2014. An automated simple algorithm for realistic pore network extraction from micro-tomography images. J. Petro. Sci. Eng. 123, 164–171. https://doi.org/10.1016/j.petrol.2014.08.020.

Rabbani, A., Mostaghimi, P., Armstrong, R., 2019. Pore network extraction using geometrical domain decomposition. Adv. Water Resour. 123, 70–83. https://doi.org/10.1016/j.advwatres.2018.11.003.

Rabbani, A., Babaei, M., Javadpour, F., 2020. A Triple pore network model (T-PNM) for gas flow simulation in fractured, micro-porous and meso-porous media. Transp. Porous Media 132 (1). https://doi.org/10.1007/s11242-020-01409-w.

Tahmasebi, P., Kamrava, S., 2018. Rapid multiscale modeling of flow in porous media. Phys. Rev. E 98, 052901. https://doi.org/10.1103/PhysRevE.98.052901.

Tan, Q., Kang, Y., You, L., Xu, F., Meng, S., 2020. A comprehensive insight into the multiscale pore structure characterization of saline-lacustrine tight carbonate reservoir. J. Petro. Sci. Eng. 187, 106744 https://doi.org/10.1016/j.petrol.2019.106744.

Tomutsa, L., Silin, D., Radmilovic, V., 2007. Analysis of chalk petrophysical properties by means of submicron-scale pore imaging and modeling. SPE Reserv. Eval. Eng. 10 (03), 285–293. https://doi.org/10.2118/99558-PA.

Valvatne, P.H., Blunt, M.J., 2004. Predictive pore-scale modeling of two-phase flow in mixed wet media. Water Resour. Res. 40, W07406. https://doi.org/10.1029/2003WR002627.

Xu, Z., Lin, M., Jiang, W., Cao, G., Yi, Z., 2020. Identifying the comprehensive pore structure characteristics of a rock from 3D images. J. Petro. Sci. Eng. 187, 106764 https://doi.org/10.1016/j.petrol.2019.106764.

Xu, Z., Lin, M., Jiang, W., Ji, L., Cao, G., 2021. Rapid multiscale pore network modeling for drainage in tight sandstone. J. Petro. Sci. Eng. 204, 108682 https://doi.org/10.1016/j.petrol.2021.108682.

Yi, Z., Lin, M., Jiang, W., Zhang, Z., Li, H., Gao, J., 2017. Pore network extraction from pore space images of various porous media systems. Water Resour. Res. 53 (4), 3424–3445. https://doi.org/10.1002/2016WR019272.